8-30-2019

Large-Amplitude Mountain Waves in the Mesosphere Observed on 21 June 2014 During DEEPWAVE: 2. Nonlinear Dynamics, Wave Breaking, and Instabilities

David C. Fritts
GATS, dave@gats-inc.com

Ling Wang
GATS

Michael J. Taylor
Utah State University, mike.taylor@usu.edu

Pierre-Dominique Pautet
Utah State University, dominiquepautet@gmail.com

Neal R. Criddle
Utah State University, neal.criddle@aggiemail.usu.edu

Bernd Kaifler
German Aerospace Center

See next page for additional authors

Recommended Citation

Fritts, D. C., Wang, L., Taylor, M. J., Pautet, P.-D., Criddle, N. R., Kaifler, B., et al. (2019). Large-amplitude mountain waves in the mesosphere observed on 21 June 2014 during DEEPWAVE: 2. Nonlinear dynamics, wave breaking, and instabilities. Journal of Geophysical Research: Atmospheres, 124, 10006– 10032. https://doi.org/10.1029/2019JD030899

Utah State University
MERRILL-CAZIER LIBRARY

Authors

David C. Fritts, Ling Wang, Michael J. Taylor, Pierre-Dominique Pautet, Neal R. Criddle, Bernd Kaifler, Stephen D. Eckermann, and Ben Liley

JGR Atmospheres

Key Points:
- Weak mountain waves at low altitudes can achieve breaking amplitudes in the mesosphere under suitable propagation conditions
- Mountain wave breaking occurs via 3-D instability dynamics predicted by high-resolution modeling in various environments
- Mountain wave instability dynamics evolve on short time scales and impose significant intermittency in wave amplitudes and momentum fluxes

Supporting Information:
- Supporting Information S1
- Data S1

Correspondence to:
D. C. Fritts,
dave@gats-inc.com

Author Contributions:
Conceptualization: David C. Fritts, Stephen D. Eckermann
Formal analysis: David C. Fritts, Ling Wang, Bernd Kaifler, Stephen D. Eckermann
(continued)

Large-Amplitude Mountain Waves in the Mesosphere Observed on 21 June 2014 During DEEPWAVE: 2. Nonlinear Dynamics, Wave Breaking, and Instabilities

David C. Fritts[1] (ID), **Ling Wang**[1], **Michael J. Taylor**[2] (ID), **Pierre-Dominique Pautet**[2] (ID), **Neal R. Criddle**[2], **Bernd Kaifler**[3] (ID), **Stephen D. Eckermann**[4] (ID), and **Ben Liley**[5] (ID)

[1]GATS, Boulder, CO, USA, [2]Center for Atmospheric and Space Science, Utah State University, Logan, UT, USA, [3]German Aerospace Center (DLR), Munich, Germany, [4]Space Science Division, U.S. Naval Research Laboratory, Washington, DC, USA, [5]National Institute of Water and Atmospheric Research of New Zealand (NIWA), Christchurch, New Zealand

Abstract Weak cross-mountain flow over the New Zealand South Island on 21 June 2014 during the Deep Propagating Gravity Wave Experiment (DEEPWAVE) led to large-amplitude mountain waves in the mesosphere and lower thermosphere. The mesosphere and lower thermosphere responses were observed by ground-based instruments in the lee of the Southern Alps supporting DEEPWAVE, including an Advanced Mesosphere Temperature Mapper, a Rayleigh lidar, an All-Sky Imager, and a Fabry-Perot Interferometer. The character of the mountain wave responses at horizontal scales of ~30–90 km reveals strong "sawtooth" variations in the temperature field suggesting large vertical and horizontal displacements leading to mountain wave overturning. The observations also reveal multiple examples of apparent instability structures within the mountain wave field that arose accompanying large amplitudes and exhibited various forms, scales, and evolutions. This paper employs detailed data analyses and results of numerical modeling of gravity wave instability dynamics to interpret these mountain wave dynamics, their instability forms, scales, and expected environmental influences. Results demonstrate apparently general instability pathways for breaking of large-amplitude gravity waves in environments without and with mean shear. A close link is also found between large-amplitude gravity waves and the dominant instability scales that may yield additional abilities to quantify gravity wave characteristics and effects.

1. Introduction

It is now understood that multiple roles of gravity waves (GWs) in atmospheric dynamics from the surface into the mesosphere and lower thermosphere (MLT) are consequences of their efficient vertical transport of energy and momentum from sources at lower altitudes into the stratosphere and the MLT. On global scales, GW/mean-flow interactions, especially by mountain waves (MWs), yield systematic forcing that weakens the zonal mean wind in the lower stratosphere and induces an equator-to-pole residual circulation and warming at higher latitudes in each hemisphere. In the MLT, GW forcing reverses the vertical shear of the zonal jets in the summer and winter mesosphere relative to the stratosphere and induces a residual circulation from pole to pole having dramatic influences on mesopause temperatures and transport at high latitudes. At equatorial latitudes, systematic GW forcing contributes to the quasi-biennial oscillation and the semiannual oscillations from the tropopause to the mesopause that also have global influences. GW interactions with tides and planetary waves (PWs) are expected to influence these motions where they achieve large amplitudes. GWs also induce turbulence and mixing that influence the mean state structure and stability from the surface to the thermosphere (see Fritts & Alexander, 2003, for a review of these influences). Importantly, none of these responses can occur without GW instabilities leading to turbulence, dissipation, and energy and momentum flux divergence. Yet the instabilities that contribute most, the environments in which they arise, and the impacts of their energy and momentum deposition are poorly constrained by atmospheric observations at present. This paper addresses these topics through interpretations of instability dynamics and their implications accompanying strong MWs observed over the Southern Alps by ground-based instruments on the New Zealand South Island (NZ SI) during the Deep Propagating Gravity Wave Experiment (DEEPWAVE) performed in June and July 2014.

Theory, modeling, and laboratory studies over many years have revealed a wide range of instabilities that accompany GWs at small and large amplitudes. GWs exhibit systematic energy exchanges via resonant and off-resonant interactions, especially parametric subharmonic instabilities that may or may not lead to turbulence (Bourget et al., 2013; Grimshaw, 1988; Klostermeyer, 1991; Lombard & Riley, 1996; McComas & Bretherton, 1977; Sonmor & Klaassen, 1997; Staquet & Sommeria, 2002; Thorpe, 1994; Walterscheid et al., 2013). Wave/mean-flow interactions at finite GW amplitudes can lead to modulational instabilities for sufficiently high intrinsic frequencies (Dosser & Sutherland, 2011; Sutherland, 2001, 2006).

At larger GW amplitudes, optimal perturbations appear to play the major roles in defining the character of instabilities leading to turbulence (Achatz, 2005, 2007; Andreassen et al., 1998; Fritts et al., 2009a, 2009b, hereafter F09a and F09b; Fruman & Achatz, 2012). GW "self-acceleration" (SA) wave/mean-flow interactions accompany the approach to overturning amplitudes for GW packets localized in altitude (and horizontally). These dynamics cause stalling of the packet propagation to higher altitudes and SA instability yielding a rapid transition to turbulence (Fritts et al., 2015). Finally, multiscale dynamics comprising superposed and interacting GW and mean fields yield variants of the above instabilities exhibiting diverse forms (Fritts et al., 2013).

Observational studies have also contributed significantly to our understanding of GW dynamics leading to instabilities and turbulence from the stable boundary layer into the MLT. They have provided key insights into instability character and environments, motivated theoretical and modeling studies, and confirmed instability pathways and consequences in many applications. As examples, radar and lidar profiling have provided evidence of the preferential occurrence of Kelvin-Helmholtz instabilities (KHI) accompanying the descending phases of larger-scale GWs (Eaton et al., 1995; Lehmacher et al., 2007; Pfrommer et al., 2009). Airborne lidars have contributed to identification of overturning implying GW breaking, as seen in the DEEPWAVE analyses of RF22 and RF23 (Eckermann et al., 2016: Fritts et al., 2018; Pautet et al., 2016). Lidars and radars have also supported interpretations of airglow imaging of instability dynamics induced or modulated by GWs (Hecht et al., 2014, 2018).

Of greatest benefit in understanding the character and evolutions of instabilities and their impacts on GW forcing or influences is imaging of these dynamics where their features and evolutions are revealed by airglow or polar mesospheric cloud (PMC) imaging in the MLT. The MLT is arguably the best region in the atmosphere to study instability dynamics that play important roles at all altitudes and in other geophysical fluids. No other altitude has tracers of small-scale dynamics enabling visualization of their evolutions in space and time. New detectors and difference imaging can reveal structures as small as ~100–200 m to highlight small-scale, rapidly evolving features in airglow imaging. Likewise, PMC imaging from the ground and the stratosphere can capture features as small as ~20–50 m because the layer of maximum PMC brightness is often as thin as ~20–100 m. Examples of these dynamics and insights from imaging include

1. KHI exhibiting secondary instabilities that point to the potential importance of background turbulence in the evolutions and scales of secondary instabilities within KH billows (Baumgarten & Fritts, 2014; Fritts, Baumgarten, et al., 2014; Fritts, Wan, et al., 2014; Hecht et al., 2014);
2. KHI exhibiting modulations of phase structures, spatial amplitude variations, and/or KH billow rotational speeds (Baumgarten & Fritts, 2014; Hecht et al., 2005, 2014);
3. GW instability structures from initial optimal perturbations to evolving "horseshoe" vortices, vortex rings, and their breakdown (Fritts et al., 1993, 2017; Hecht et al., 1997, 2018; Miller et al., 2015; Swenson & Mende, 1994; Yamada et al., 2001);
4. Instabilities arising in idealized GW breaking and multiscale dynamics simulations, including GW breaking fronts, intrusions, and cusp-like breaking (Fritts et al., 2017; Miller et al., 2015);
5. Evidence of strong interactions among adjacent KH billows initiated by vortex "tubes" and "knots" previously seen only in laboratory shear flows (see Thorpe, 1987, 2002).

DEEPWAVE was conceived and designed to enable exploration of the propagation of GWs arising from various sources, but especially by flow over significant orography, and their interactions, instabilities, and influences in varying environments from the surface into the MLT. It involved two research aircraft, the NSF/NCAR Gulfstream V (GV) and the German Aerospace Center (DLR) Falcon, both equipped with in situ and remote-sensing instruments. GV Rayleigh and resonance lidar profiling extended from ~25 to 105 km and an Advanced Mesosphere Temperature Mapper (AMTM) imaged temperatures at ~87 km along and

across the GV flight track. DEEPWAVE airborne measurements were augmented by a large suite of ground-based instruments on NZ SI and Tasmania (see Fritts et al., 2016, 2018, and Taylor et al., 2019, hereafter T19, for details and the relationship of DEEPWAVE to previous MW and more general GW studies). Instruments of relevance for this study include a ground-based AMTM and a Rayleigh lidar at Lauder, NZ in the lee of the S. Alps (Fritts et al., 2016; Kaifler et al., 2015).

DEEPWAVE observations have been employed for multiple analyses of MW dynamics extending into the stratosphere and MLT to date. Strong winds over the S. Alps during GV research flight 12 (RF12) on 29 June and on GV research flight RF16 and Falcon research flights 4 and 5 (FF04 and FF05) on 4 July were found to yield strong MW forcing and significant MW breaking in the stratosphere, to also allow MW penetration into the MLT despite breaking in the stratosphere, and apparent secondary GWs (SGWs) arising due to MW breaking at lower altitudes (Bossert et al., 2017; Bramberger et al., 2017). Weak cross-mountain flow prior to RF22 on 13 July was also found to yield very large MWs in the upper stratosphere and MLT, and strong breaking and SGW generation under conditions allowing largely linear MW propagation throughout the stratosphere (Bossert et al., 2015; Fritts et al., 2018; Heale et al., 2017). Conversely, strong flow over the low Auckland Islands terrain during RF23 on 14 July yielded a deep "ship wave" GW response exhibiting breaking in Na lidar and AMTM observations in the MLT (Broutman et al., 2017; Eckermann et al., 2016; Pautet et al., 2016).

MLT vertical fluxes of horizontal momentum (MFs) were inferred for MWs and secondary GWs based on individual GW amplitudes (Bossert et al., 2015; Fritts et al., 2018) and using a spectral assessment along the GV flight tracks (Bossert et al., 2018) for RF22 on 13 July. These revealed very large local MFs of $\sim$300–700 m^2/s^2 to be associated with MWs having $\lambda_h \sim$60–75 km, based on Na mixing ratio displacements centered at $\sim$76–79 km. Spectral MF estimates averaged along the GV flight track were $\sim$10 times lower for larger estimated MW $\lambda_h \sim$80–120 km at somewhat higher altitudes, and nearer the estimated MW critical level at $\sim$90 km. T19 performed similar assessments of MW MFs using DEEPWAVE ground-based measurements over Lauder and observed three successive maxima of $\sim$600–800 m^2/s^2 that were among the largest ever observed in the MLT at any site of $\sim$900 m^2/s^2 (see Fritts et al., 2002; Fritts, Pautet, et al., 2014).

Not addressed in any DEEPWAVE studies to date, despite evidence for such in GV AMTM and OH imaging on GV flights RF12, RF16, RF22, and RF23 described in papers cited above, are the character and scales of instability dynamics accounting for MW breaking in the MLT. This is due, in part, to earlier DEEPWAVE foci on MW dynamics and SGW implications themselves. Another reason is the inability to achieve the same high spatial resolution by OH imaging from the GV as is possible from the ground. However, identification of instability dynamics scales and character provides key guidance on the intensities and potential influences of the underlying GW field, as described below and in other applications by Fritts et al. (2017, 2018, 2019).

Our purpose here is to examine the formation and evolution of instability dynamics accompanying a large amplitude, apparently overturning MW observed in the MLT by the AMTM and from $\sim$50 to 90 km by the Rayleigh lidar at Lauder, NZ on 21 June 2014. T19 employed these observations, and OH and OI airglow imaging by an All-Sky Imager and radial winds measured by a Fabry Perot interferometer (FPI) at the Mount John Observatory (MJO) on SI to examine the larger-scale MW dynamics. The OH and OI layers were assumed to have maximum brightness at $\sim$82 and 92 km, respectively, given the OH layer seen by SABER on this night. During the strongest responses, the MW field exhibited slowly varying phase motions, westward propagation in largely eastward winds, horizontal scales of $\sim$12–90 km, and implied very large MFs at the OH layer. These observations also revealed strong overturning of the larger-scale MWs, yielding sawtooth patterns in the temperature (T) fields, with large positive and negative perturbation temperatures, T', at the east and west (E/W) edges, respectively, of the sawtooth features following the descending MW phases (see further discussion by T19). Strong overturning implies a potential for significant instabilities, turbulence generation, and MW energy and momentum deposition, and these instability dynamics are the foci of this paper.

Here we identify the dominant instabilities accompanying MW breaking observed in the MLT during the 21 June 2014 DEEPWAVE event, their occurrence, scales, and evolutions within the larger-scale MWs, and their implications for MW amplitudes, dissipation, and momentum deposition. Relations among MW and mean flow parameters that will be useful in our analysis and our methods for approximating OH airglow brightness using our modeling are presented in section 2. Section 3 employs AMTM and Rayleigh lidar

data obtained at Lauder on SI and FPI data from MJO to summarize the MW evolution spanning the strong instability dynamics observed on this night. The major MW instability events and their dynamics and implications are described in section 4. A discussion of our results and our summary and conclusions are provided in sections 5 and 6, respectively.

2. GW Parameters and Representation and Simulations of Airglow Brightness

2.1. GW Parameters and Relations

Relations among the GW and environmental parameters are presented here for convenience. Assuming linear GWs, weak mean gradients, negligible Coriolis influences, and propagation in the (x,z) plane, the linearized perturbation equations are as follows:

$$ku' + mw' = 0 \tag{1}$$

$$p' = -\rho_0\left(N_0{}^2 - \omega_i{}^2\right)w'/m\omega_i = \rho_0\omega_i u'/k \tag{2}$$

$$\theta'/\theta_0 = -iN_0{}^2 w'/g\omega_i = iN_0{}^2 u'/g\left(N_0{}^2 - \omega_i{}^2\right)^{1/2} \tag{3}$$

The nonhydrostatic dispersion relation for such GWs is

$$m^2 = N^2/(c-U)^2 - k^2 - 1/4H^2 \tag{4}$$

In the hydrostatic GW limit, the first term on the right-hand side of equation (4) dominates, yielding the following expressions to a good approximation:

$$\lambda_z = 2\,\pi(c-U)/N_0 \tag{5}$$

$$|u'| = (g/N_0)|T'/T| \tag{6}$$

$$|du'/dz| = |mu'| = aN_0, \text{where } a = |(d\theta'/dz)|/(d\theta_0/dz) = |u'/(c-U)| \tag{7}$$

In the above, u, w, T, θ, p, and ρ are the horizontal and vertical wind components, temperature, potential temperature, pressure, and density fields, respectively, (U,V) and "0" subscripts denote mean fields, primes denote GW perturbations. The GW horizontal and vertical wave numbers and wavelengths are related as $k = 2\pi/\lambda_x$ and $m = 2\pi/\lambda_z$, respectively, the intrinsic and ground-based GW frequencies are related as $\omega_i = \omega - kU = k(c - U)$, where c is the horizontal phase speed in the plane of propagation, $\theta = T(p_0/p)^{2/7}$, $N^2(z) = (g/\theta)(d\theta/dz)$, with mean buoyancy frequency $N_0(z)$ evaluated for $\theta = \theta_0$, g is gravitational acceleration, and $a = 1$ is the nondimensional GW amplitude at incipient overturning. With scale height H, $\lambda_z << 4\pi H$ for hydrostatic GWs and m is real (imaginary) for vertically propagating (evanescent) GWs, implying different relative phases in equation (1) in the two cases. Finally, instability and turbulence dynamics require a sufficiently large GW Reynolds number, defined as $Re = |c - U|\lambda_z/\nu\nu\nu = \lambda_z{}^2/\nu\nu T_b$ (Fritts et al., 2009a) for hydrostatic GWs, kinematic viscosity, ν, and buoyancy period, $T_b = 2\pi/N_0$.

2.2. Representation of Airglow Brightness

As in Fritts, Pautet, et al., 2014, Fritts et al., 2017), we assume that local OH emission intensity or "airglow brightness", I, variations depend only on advection. Such an assumption for GW motions varying over multiple T_b (as in our study, where the MW period is ~3–4 T_b) is surely not justified, given multiple modeling studies showing chemical time scales ~4–6 min (Makhlouf et al., 1995; Snively et al., 2010). This suggests that the larger-scale MWs will have airglow responses close to equilibrium. However, instability dynamics of interest here evolve on substantially shorter time scales, suggesting that evolutions of 3-D instability features will be revealed to a large degree by dynamical advection at smaller scales. As will be seen below, the transition from an initial coherent vortex ring to well-developed turbulence accompanying GW breaking occurs in less than 1 T_b (F09b), suggesting advection to be a valid assumption in these applications.

This advection acts on an initial distribution expressed in terms of an undisturbed initial $\theta_0(z)$ as

$$I(z) = I_0 \exp\left[-(z-z_{OH})^2/2\sigma_z^2\right] = I_0 \exp\left[-(\theta-\theta_{OH})^2/2\sigma_\theta^2\right] \tag{8}$$

Here $\theta = \theta_{OH}$ and $I = I_0$ at $z = z_{OH}$, $\sigma_z = z_{FWHM}/2(2\ln2)^{1/2}$ corresponds to an undisturbed $I(z)$ having a typical full width-half maximum (FWHM) of $z_{FWHM} \sim 7$ km based on SABER profiles shown by T19, and we assume $d\theta_0/dz$ is approximately constant across the OH layer FWHM. The latter assumption is exact for the incompressible DNS (with $\theta = T$) employed below to approximate integrated OH layer $I(x,z)$ and $I(x,y)$ to aid our interpretation of AMTM observations of MWs and their associated instabilities.

2.3. Simulations of Airglow Brightness

To improve our ability to recognize instability dynamics accompanying MW breaking, we employ equation (8) for the OH intensity for applications in idealized DNS of GW breaking in unsheared and sheared environments. Unsheared DNS include those for $a = 0.9$ and 1.1 and $\omega_i = N/3.2$, $N/2$, and $N/1.4$ (F09a; Fritts et al., 2009b, hereafter F09b). These flows are not representative of mean flows implied by Navy Global Environmental Model (NAVGEM) reanalysis at ~80–90 km at most times on 21 June (see Figure 3 below). However, multiple other applications for sheared mean flows have revealed that GW breaking dynamics inevitably involve the underlying vortex (and vortex ring) dynamics found to occur in these cases. To approximate these dynamics, we also employ results from a DNS of a GW exhibiting initial instability in a mean wind shear for $\lambda_x = 20$ km and $\lambda_z \sim 3$ km at the time in the evolution at which these fields are employed.

For the various DNS noted above, we assume an undisturbed OH brightness layer described by equation (8) to have been present prior to the GW and resulting instability and turbulence dynamics. Airglow brightness fields illustrating the responses to the various DNS instability evolutions will be discussed below, as appropriate for the instability events examined.

3. Mountain Wave Evolution on 21–22 June

The MW evolution over SI on 21–22 June of relevance to our analysis was observed primarily by the AMTM and the Rayleigh lidar at Lauder. The AMTM defined the horizontal structure of the MW field in OH layer $I(x,y)$ and $T(x,y)$ in an ~200 × 149 km field of view (FOV; Figure 1). The lidar defined the MW $T(z,t)$ at altitudes from ~30 to 90 km (Figure 2). Zonal winds were obtained from a high-altitude (T119L74) hybrid four-dimensional, variational (hybrid-4DVAR) reanalysis using NAVGEM described by Eckermann et al. (2018). The winds presented here were interpolated onto geometric height surfaces, averaged from 166–173°E and 43–47°S over Lauder, and obtained at hourly resolution.

OH T and I keograms shown by T19 reveal that the strong MW breaking event observed on 21 June accompanied a large-scale warming and brightening of the OH emission layer that extended from ~10:30 to 12:30 UT. These variations exhibit a dominant ~6-hr period that suggests a larger-scale GW or tidal influence on the MW responses seen in the OH brightness and temperature fields. Also revealed in the T keogram is a strong, transient ~3- to 4-hr response centered on this event (see the T minima at ~9–10 and 13 UT). The FPI at MJO observed enhanced zonal winds at the OH layer extending from ~11 to 12 UT at the peak of this event (see T19), though the FPI winds at the OH layer were ~10–15 ms^{-1} larger than those suggested by NAVGEM reanalysis at these times (see Figure 3). Comparing the T and $u = U + u'$ fields shown by T19 for the longer interval, we see that the T maximum lagged the u maximum (and downward w'). This suggests that a ~3- to 4-hr GW was propagating largely toward the west (and upward), such that its T maxima followed the descending eastward u maxima. It is this larger-scale u maximum that appears to have allowed MWs to penetrate to higher altitudes and be viewed in the OH layer during this interval (also see the discussion of NAVGEM winds below).

Prior to ~10 UT on 21 June, neither the AMTM nor the lidar data exhibited any indication of MWs in the mesosphere. See, for example, the lack of coherent features at higher altitudes and the apparent downward phase progression above ~45 km extending to ~9 UT in the lidar $T(z,t)$ cross section at left in Figure 2a. Significant MW responses below and above 80 km began to appear in AMTM images and lidar profiles at ~10 UT, shortly before the first images at top in Figure 1 (see the emerging warm layer at ~87 km in Figure 2a). The AMTM initially revealed emerging weak, quasi-stationary MWs having phases initially aligned approximately along the SW-NE direction.
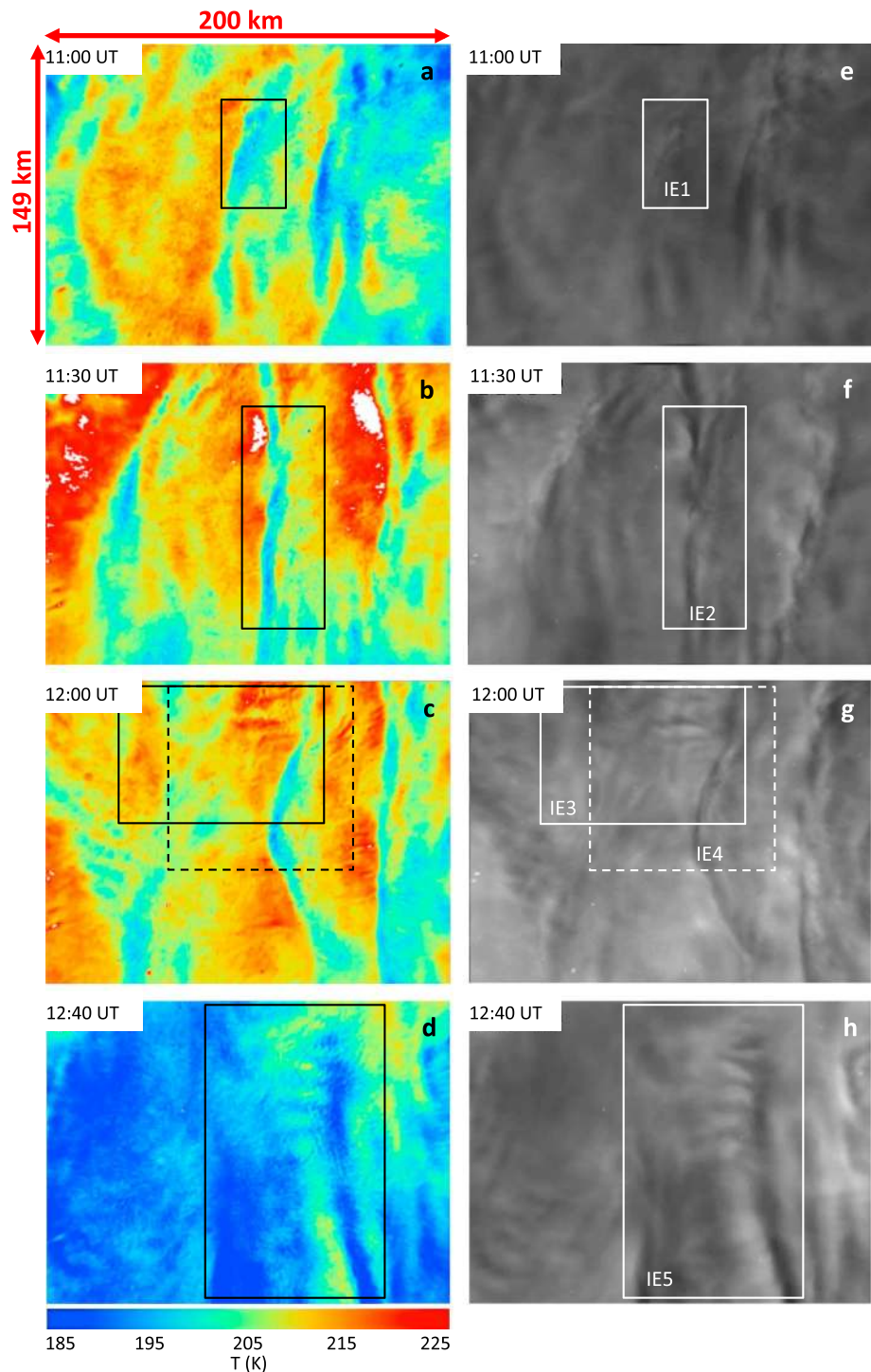
Figure 1. (left and right) Flat-fielded AMTM $T(x,y)$ and $I(x,y)$ fields showing the evolution of the MW field over Lauder, NZ on 21–22 June 2014 viewed from above. MWs have $\lambda_h \sim 10$–90 km, exhibit slow phase variations in time as the major contributing λ_h vary, and reveal strong overturning throughout this interval. Inset rectangles show the subdomains for the five instability event assessments.

By 11 UT, MW amplitudes had increased further, phases were more nearly aligned N-S, and there were distinct apparent MWs having $\lambda_x \sim 12$–90 km. Amplitudes increased further by 11:30 and 12 UT, at which times clear saw-tooth patterns at $\lambda_x \sim 40$–90 km were seen in T and to a lesser degree in I. These included MW phases
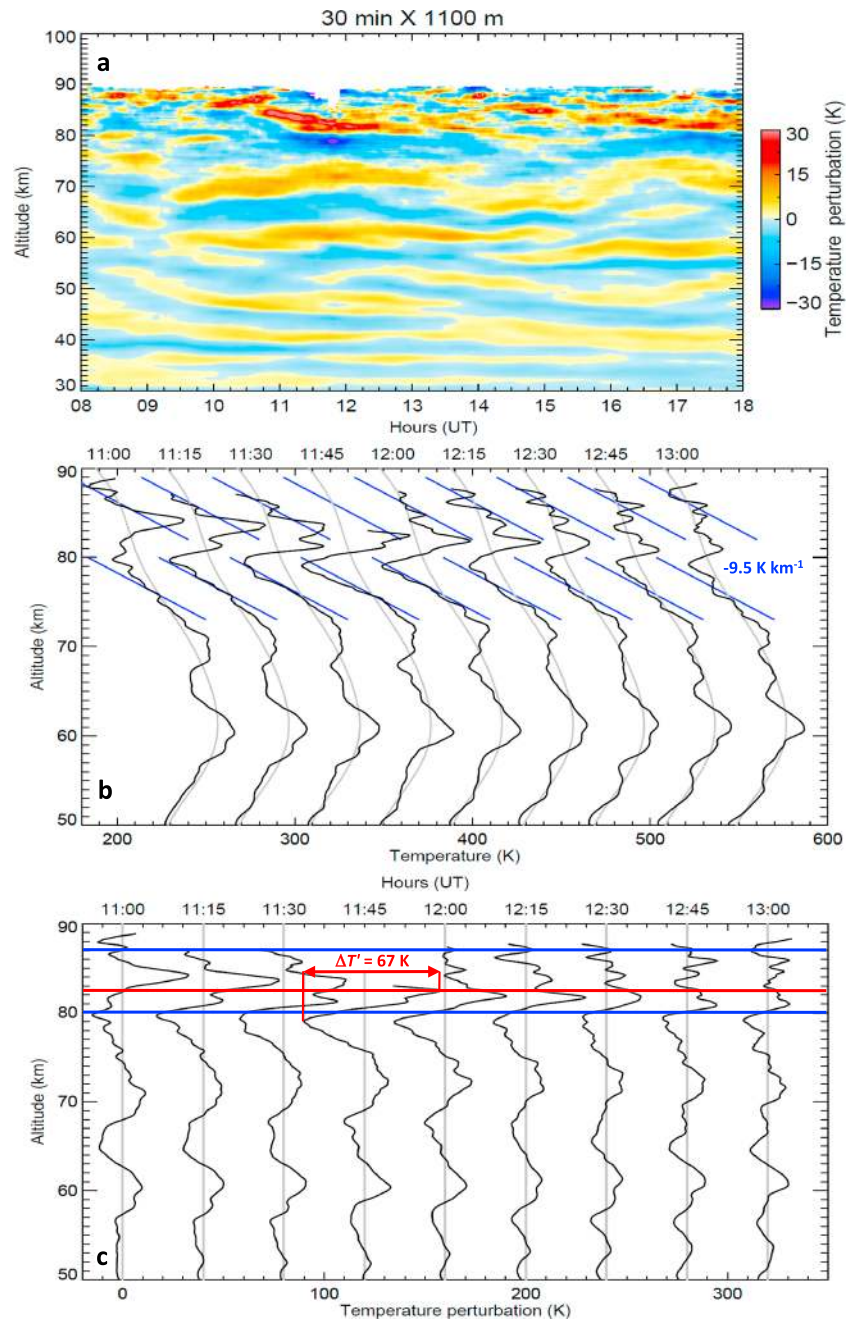
Figure 2. (a) $T(z,t)$ with 30-min and 1,100-m averaging for 10 hr showing the evolving MW field from the lower stratosphere to the upper mesosphere. (b and c) $T(z)$ and $T'(z)$ profiles with 30–min and 900-m averaging. Shown at center is the adiabatic lapse rate in blue; shown at bottom are the OH layer peak (red line) and the z_{FWHM} boundaries above and below (blue lines). Note the superadiabatic lapse rates, very large T', and decreasing λ_z above 75 km at earlier times, and the layered, more stable profiles above 80 km thereafter. Smoothed nearby SABER temperature profiles were employed to define the mean temperature profile to avoid biases by stationary MWs.

with relatively uniformly increasing T from west to east separated by large, rapid decreases of T in crossing to the next warm phase. Mean T and MW amplitudes at the OH layer decreased strongly after ~12 UT, but MWs persisted at larger and smaller scales beyond 15 UT (see the lidar cross sections in Figure 2a).

Throughout this evolution, both systematic and variable motions of the phase structures and variations in MW amplitudes were seen at large and small λ_x. AMTM images also revealed multiple T' and I' perturbations in the AMTM images having horizontal scales of ~3–10 km and more nearly zonal alignments that will be
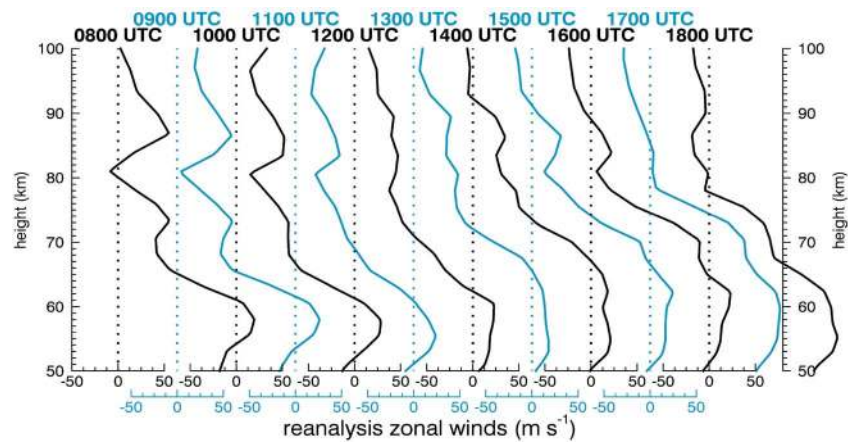
Figure 3. NAVGEM reanalyzed zonal winds as a function of height and time on 21 June 2014 over Lauder. Wind profiles were averaged from 166–173°E and 43–47°S. See text for additional details.

seen below to provide evidence of MW breaking (see T19 for additional details). These responses, and the Lauder lidar $T(z)$, indicate overturning of the larger-scale MWs; see the regions of superadiabatic $dT/dz < -g/c_p$ in Figure 2b. These yield strong MW breaking and instability dynamics to be addressed in detail below. A movie of the AMTM $I(x,y)$ field from 10 to 14 UT is shown for reference in AMTM_I.mp4 (see supporting information).

NAVGEM reanalysis zonal winds in Figure 3 reveal near zero values at ~80 km at 8 and 9 UT, which would be expected to prevent MW penetration to higher altitudes (via critical-level filtering and/or enhanced MW breaking at lower altitudes), as observed. NAVGEM winds at ~75–85 km increased thereafter and remained at ~40–50 ms^{-1} above ~82 km and weakened somewhat approaching 90 km from 10 to 13 UT. The stronger eastward zonal winds during this interval coincide closely with the strongest AMTM and lidar MW T' responses at these times. The increasing zonal winds below ~75 km also imply a conducive environment for MW propagation to these altitudes after ~12 UT, despite the weakening winds near ~90 km thereafter.

Using the lidar $T(z)$ (see Figure 2b) and nearby SABER profiles shown by T19, we estimate a mean $dT/dz \sim -2.5$ Kkm^{-1} yielding $N_0 \sim 0.018$ s^{-1}. Equation (5) then implies a local $\lambda_z \sim 14$–17 km for $U \sim 40$–50 ms^{-1}. This λ_z cannot be confirmed with lidar $T'(z)$ measurements (see the profiles in Figure 2c), as they did not extend above 89 km. However, the lidar dT/dz and $T' \sim 25$–30 K at these times (see Figures 2b and 2c profiles from 11:15 to 12 UT and possibly later) imply MW overturning and vertical displacement amplitudes of $\delta z \sim 3.6$–4.3 km that are consistent with MW overturning ($a > 1$) for the estimated λ_z, which occurs at amplitudes $\delta z > \lambda_z/2\pi$ from equation (7).

Direct estimates of MW λ_z below ~85 km are enabled by the lidar $T(z,t)$ cross section from 8 to 18 UT in Figure 2a and the $T'(z)$ profiles from 11 to 13 UT in Figure 2c. These reveal MW T' perturbations that are fairly constant in time and altitude up to ~75 km, above which they exhibit larger amplitudes and nearly adiabatic lapse rates from ~11:15 to 12:30 UT. There is also evidence of variable λ_z that may be an indication of variable propagation directions, as noted by T19 and in the AMTM discussion above. MW T' maxima undulate in altitude more significantly at ~65–75 km at an apparent period of ~6 hr. The large upward displacement of the warm phase near 73 km at ~17 UT (and maximum large-scale MW $\lambda_z \sim 15$ km) coincides with the maximum NAVGEM U at ~70 km, consistent with equation (5) assuming zonal propagation. Changing dominant propagation directions towards (away from) the maximum mean wind will also result in larger (smaller) λ_z, according the equation (5). Given our lack of MW phase information in the stratosphere and lower mesosphere, however, we cannot distinguish among these influences.

An opposite altitude variation in the MW warm phase near 80 km is also observed. This is seen to yield maximum T' and dT'/dz amplitudes and minimum λ_z at ~11–12 UT as NAVGEM U increases to ~50 ms^{-1} at ~80 km and at ~17–18 UT following large U decreases. These variations suggest influences by a GW or

tide having λ_z~20–30 km and a period near ~6 hr, as also seen in the AMTM keograms discussed by T19. Such influences could also contribute to the decreasing λ_z with time noted by T19.

The MW λ_z below ~85 km is defined by the successive large-scale T' maxima noted above, yielding estimates ranging from ~13 km at 11 UT to ~10 km at ~12 UT and thereafter. These λ_z estimates are somewhat less than implied by the NAVGEM zonal winds above ~82 km, which should be smaller, given the expected decreasing zonal winds with increasing altitude. A plausible explanation is that NAVGEM winds are somewhat overestimated because NAVGEM does not fully resolve and parameterize the local MW momentum deposition that must accompany strong MW breaking and dissipation over SI during this event. Indeed, the lidar $T(z)$ suggest that MW momentum deposition likely begins as low as ~75 km (see the weak superadiabatic lapse rates in Figure 2b at ~11:30–12 UT) and increases strongly with altitude, given the stronger superadiabatic lapse rates above ~82 km from ~11 to 12 UT and perhaps thereafter and the strong and large-scale instability dynamics to be discussed below. If this is a reasonable explanation, it implies that MW momentum deposition yields a mean reduction in U of up to ~30% at these altitudes, with the larger flow decelerations likely occurring at higher altitudes accompanying stronger instabilities.

The AMTM was likely largely insensitive to potential instability dynamics below ~80 km, given the expected peak OH brightness at ~82 km. In contrast, the AMTM was likely increasingly sensitive to instability dynamics above ~82 km with time, given the apparent descent of the more strongly unstable layer initially above ~85 km.

The evolution of the overall MW event is generally consistent with the evidence of instabilities in the AMTM and lidar measurements. The most intense instabilities seen in the AMTM images occurred at multiple sites from ~11 to 13 UT, but localized MW responses and instabilities also extended further in time at apparently lower altitudes. Specific features of relevance to our instability assessments below include the following:

1. decreasing λ_z above 70 km from ~13 km initially to ~10 km at ~12 UT and thereafter,
2. strong positive dT'/dz and increasingly strong dT/dz at ~80–85 km up to ~12 UT,
3. large, sharp, positive T' ~25–30 K descending from ~87 to ~82 km as λ_z decreases,
4. superadiabatic lapse rates, $dT/dz < -9.5$ Kkm^{-1}, above the T' maxima, initially above ~87 km but decreasing in altitude to ~82 km by ~13 UT as λ_z decreases,
5. additional approximately adiabatic (or superadiabatic) lapse rates at ~75–80 km extending from ~11:30 to 12:30 UT, and
6. increasing fine structure in $T'(z)$ from ~80 to 88 km as the strong instabilities subside.

As will be seen below, AMTM sensitivity to MW instability dynamics was impacted by the OH layer altitude relative to the unstable phase of the MW field, its variation in the horizontal, and its descent with time. The OH weighting in altitude throughout the evolution is illustrated in Figure 2c, where red (blue) lines show the peak (FWHM) altitudes based on downwind SABER and mean lidar $T(z)$ profiles. The asymmetry in the spacings of the blue lines is due to the larger observed FWHM depth above than below the layer peak (see T19). The descent of the warm MW phase with time that accompanied decreasing λ_z above ~70 km accounted for the change from colder to warmer AMTM T at the center of the images from 11 to 11:30 UT, near which the OH weighting was colocated with the local $T(z)$ maximum. The continuing descent of the primary MW phase yielded increasing sensitivity to the MW instabilities thereafter. This began with sensitivity to the lowest, latest instabilities, followed by sensitivity to initial instabilities arising at higher altitudes, that is, sweeping from lower to higher altitudes within the most unstable MW phase as it descends with time.

Turning now to the AMTM temperatures, we expect that the AMTM measured <T'>, where angle brackets denote an average over the OH layer, underestimate the true MW amplitudes, T', where λ_z is small (Fritts, Pautet, et al., 2014). As described by T19, sawtooth patterns in the T fields suggest significant MW overturning at λ_x~40–90 km during the larger MW responses approaching 11:30 UT and thereafter, and this is confirmed by Lauder lidar measurements shown in Figure 2. In such cases, accurate T and I assessments accompanying strong advection and overturning must be modeled directly. Modeling the MW responses during DEEPWAVE event RF22 by Heale et al. (2017) revealed strong variations in the OH T and I profiles throughout the MW phase and expected underestimates of T' and I' due to variable OH emission maxima. In the current event, maximum MW amplitudes as seen by the AMTM were

achieved approaching 11:30 UT, ~30–60 min after comparable T' maxima were seen by the Lauder lidar above the peak of the OH layer. AMTM T' maxima were also ~20% or smaller than the maxima seen by the lidar and decreased with the lidar T' maximum at ~82 km after ~12 UT.

The variations of the MW wavelengths, amplitudes, phases, and orientations on short and longer time scales almost surely arose due to a combination of the following:

1. variable forcing conditions modulating the MW field and orientations as noted above,
2. refraction by, and interactions with, the mean wind and temperature fields (including momentum deposition) from lower altitudes into the mesosphere, and
3. nonlinear dynamics of, and interactions among, MWs at various scales.

As an example, T fields shown in Figure 1 at 11:30 and 12 UT suggest potential influences by MWs having λ_x~100 km or larger (see the larger T at the first and third warm phases of the λ_x~70-km MW at 11:30 UT and the larger apparent warm phase at upper left at 12 UT). These are likely to also be MWs because the phases meander back and forth in the zonal direction, but there is no evidence of systematic propagation toward east or west at larger scales, apart from that attributed to the decreasing λ_z noted in the discussion of the lidar data.

Apparent MWs having λ_x <20 km seen throughout the evolution in Figure 1 are more of a mystery. The dispersion relation, equation (4), reveals that MWs having λ_x <30–40 km would be evanescent below ~60 km due to $(c\text{-}U)$ ~100 ms^{-1} or larger and N_0 ~0.02 s^{-1}; for example, see the $U(z)$ and $T(z)$ below 60-km altitude in Figures 2b and 3. This explains the predominance of vertically propagating (i.e., over-turning) MW λ_x ~40–90 km in the AMTM images. At OH layer altitudes (~80–87 km), U ~50 ms^{-1} and N_0 ~0.018 s^{-1} (see Figures 2b and 3) imply that MWs having λ_x ~15 km or less remain evanescent. This implies that the observed structures must have either (1) tunneled into the MLT from orographic sources at lower altitudes and remained evanescent at the OH layer for the smaller λ_x, (2) tunneled into the mesosphere and become vertically propagating nonhydrostatic MWs for λ_x ~20 km, or (3) arisen as secondary MWs or instability features due to nonlinear interactions among the larger-scale propagating MWs at lower altitudes.

The first of these options appears highly unlikely because of the close alignment of the λ_x ~12 km evanescent MW phase structures with those of the vertically propagating MWs having λ_x ~40–90 km seen in the AMTM images (e.g., see the bottoms of Figures 1b and 1f). This would seem unlikely to have occurred if the observed phases at the OH layer were a linear superposition of MWs excited at different scales and orientations from differing terrain features, surface flows, and vertical group velocities.

MWs having λ_x~20 km generated by flow over the SI terrain must also have been evanescent below ~60 km but were likely vertically propagating, for example, $m^2 > 0$ in equation (2), at ~80- to 90-km altitudes from ~11 to 13 UT. Such MWs would not necessarily have phases aligned with the larger-scale MWs. They would, however, have had dT'/dz and du'/dz that likely contributed to superposed MW environments inducing local instabilities during this MW event.

Finally, interactions among, or nonlinear responses to, larger-scale MWs are certain to have occurred at higher altitudes in such a large-amplitude MW environment. The 2-D and 3-D modeling studies (Fritts et al., 2015; Heale et al., 2017; Satomura & Sato, 1999) reveal that secondary GWs or coherent quasi-2-D instabilities readily arise at smaller scales and have phase alignments parallel to the larger-scale MWs in many cases. Such responses easily span the range of smaller MW scales seen in Figure 1, λ_x~10–20 km or larger and may thus have vertically propagating (evanescent) structure at larger (smaller) λ_x, both of which would yield T' and u' and their gradients that may contribute to local, superposed MW environments enabling smaller-scale instabilities and MW breakdown.

4. Instability Dynamics, Events, and Implications

As noted above, idealized and multiscale modeling and imaging of airglow and PMCs with high spatial resolution have revealed a number of types of instabilities accompanying GWs having large amplitudes. These include (1) counter-rotating vortices aligned along, or oblique to, superposed GWs and mean shears, (2) vortex rings accompanying the transition to turbulence, (3) KHI occurring where GWs enhance mean shears

confined to thin sheets near their maximum upward displacements, (4) intrusions due to superposed lower-frequency motions, and (5) wave-wave interactions that alter the local environments but may not contribute directly to turbulence. Additionally, wave/mean-flow interactions imply SA instabilities (see above). Of these, the first three and the 2-D wave-wave and wave/mean-flow interactions appear most likely to occur in a field of superposed higher-frequency MWs (e.g., Dosser & Sutherland, 2011; F09a, b, 2015, 2016), given the large MW amplitudes and momentum fluxes inferred by T19. Lastly, we expect secondary GW generation accompanying localized MW breaking, and these can occur on larger and smaller scales than the breaking MWs.

Counter-rotating vortices yield warming between them where motions are downward and imply bands spaced by up to ~0.5 λ_z, depending on environmental and GW parameters (Andreassen et al., 1998; F09b). Thus, we expect N-S spacings of roughly E-W enhanced T and I bands at scales up to ~5–7 km for the MWs discussed here, with narrower (wider) bands likely occurring for smaller (larger) λ_z, larger (smaller) a, strongly (weakly) sheared horizontal flows, and smaller (larger) T' and I'. The downward motions induce stretching and intensification of the opposite spanwise vortex sheets below, and these structures link to form a succession of vortex rings along the GW phase that expand in time and advect upward at the maxima of u' and w' along c, but at a horizontal speed $<c$ because these instabilities have already reduced the GW amplitude, yielding an eastward drift in the MW here. The resulting vortex rings yield plunging motions in the direction of horizontal GW propagation that yield adiabatic warming. Thereafter, strong interactions among adjacent vortices induce perturbations of the various vortex structures that drive their turbulent fragmentation and collapse to smaller scales that span ~1 T_b or less. See, for example, the much shorter time scale for evolution of the vorticity field than for the MW; see the left panels of Figures 4 and 5 (also see Andreassen et al., 1998; F09b). Corresponding $I(x,y)$ fields obtained as described above centered at an altitude that highlights the vortex ring impacts on the OH layer are shown in the right panels of Figures 4 and 5. To show the vortex ring influences on T and I in the vertical, we show streamwise-vertical cross sections of T, u, and I for the DNS in Figure 6. Spanwise-mean fields at 22 T_b are shown in Fig 6b-d; cross sections of u' and I' at 22 (23) T_b are shown in Figures 6e and 6f (6g and 6h) for reference below.

New DNS of GW breaking for higher ω_i have revealed the same tendency for more rapid evolutions with increasing initial amplitudes as reported in F09b. Increasing ω_i was found to yield (1) increasing spanwise locations of vortex responses with increasing altitude at the same GW phase, (2) greater complexity of the vorticity fields having larger and smaller vortex rings with increasing ω_i, and (3) more rapid and vigorous evolutions than found by F09b for $\omega_i = N/3.2$. Vortex structures arising in the new DNS for $\omega_i = N/2$ and $N/1.4$ and $a = 0.9$ and 1.1 are shown in (x',y') planes at $z' = Z/2$ at times of initial vortex rings at left in Figure 7. Corresponding I fields for an airglow layer centered in the GW field at 0.6 λ_z above the origin of the GW breaking flows (the lower right corners of the images in Figure 6 for reference) are shown in the right panels of Figure 7.

Summarizing the major responses at larger ω_i, the vorticity cross sections (Figure 7, left) reveal that increasing ω_i leads to increasingly oblique vortex sheet alignments and ring formation relative to the streamwise direction, decreasing vortex sheet separations and ring diameters with increasing ω_i and a, and more rapid evolutions to turbulence (not shown). The vertically integrated I fields (Figure 7, right) reveal that vortex rings continue to yield clear signatures for all these cases but that their streamwise and spanwise spacings decrease with increasing ω_i and a. Specifically, spacings between adjacent brighter and darker features at the same altitude yield a staggered spacing of ~1.1λ_z for $\omega_i = N/3.2$ (see the right panels of Figures 4 and 5), but these decrease to ~0.9λ_z for $\omega_i = N/2$ and ~0.4λ_z for $\omega_i = N/1.4$ (see the right panels of Figure 7). The features at larger ω_i also reflect the increasingly oblique alignments of the vortex ring rows.

Finally, we include examples of initial instability forms accompanying a shallower GW in a mean shear, given the evidence for smaller GW amplitudes accompanying decreasing mean winds at later times described by T19 (see Figures 1e–1h). Results from a representative simulation employing the anelastic finite-volume model described by Lund and Fritts (2012) for a GW having $\lambda_h = 20$ km and $\lambda_z \sim 3$ km in a mean shear of dU/dz ~0.0013 s^{-1} are shown in Figure 8. The upper panels show the $\theta(x,z)$ field and $U(z)$ profile at the time of the corresponding simulated brightness images below, shown for several
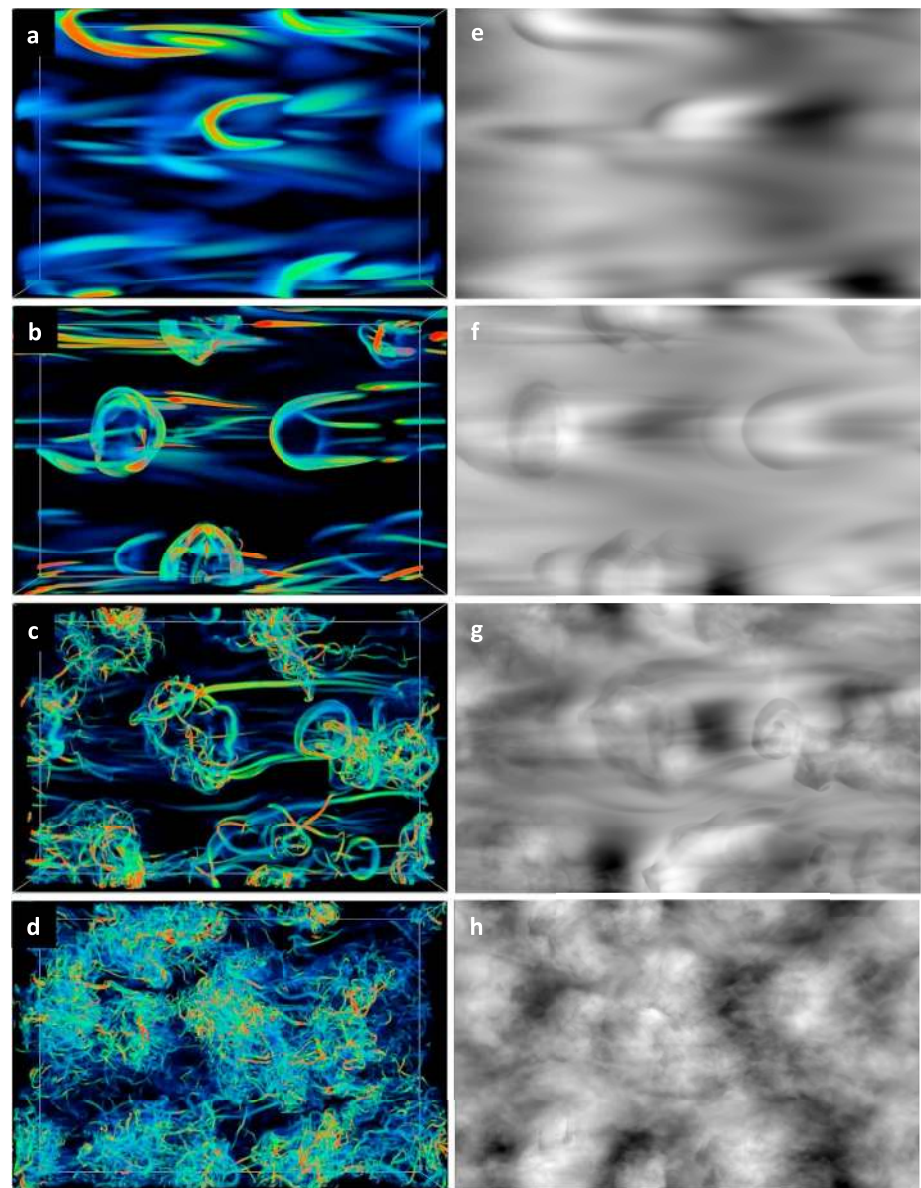
Figure 4. (left) The 3-D volumetric vortex dynamics and (right) simulated OH airglow brightness viewed from below in a numerical model of GW breaking for $a = 0.9$ and $\omega_i = N/3.2$ in an environment with uniform N and U at 20, 21, 22, and 23 T_b (top to bottom) spanning the transition to vortex rings and turbulence (after F09b). A simulated OH layer having z_{FWHM} ~7 km in equation (8) centered at the altitude of the vortex rings in panel b was assumed for the panels at right.

different altitudes within the GW field. Applications of these results are discussed in the interpretation of instability dynamics below.

Several features are robust across these various DNS in our applications here. There is an apparently quite general pathway from initial ~2-D, high-frequency GWs through initial counter-rotating, nearly horizontal vortices through vortex rings, and a rapid cascade to turbulence (at least for the *Re* considered) in both unsheared and sheared environments. In all cases shown, there is a clear tendency for vortex ring dynamics to lead to staggered modulations of I in the spanwise direction with increasing ω_i and a. There are, however, differences in the alignments of, and spacings between, initial vortex sheets and vortex ring diameters with varying ω_i and a that may enable a distinction among these GW breaking parameters where imaging resolution is sufficiently high.
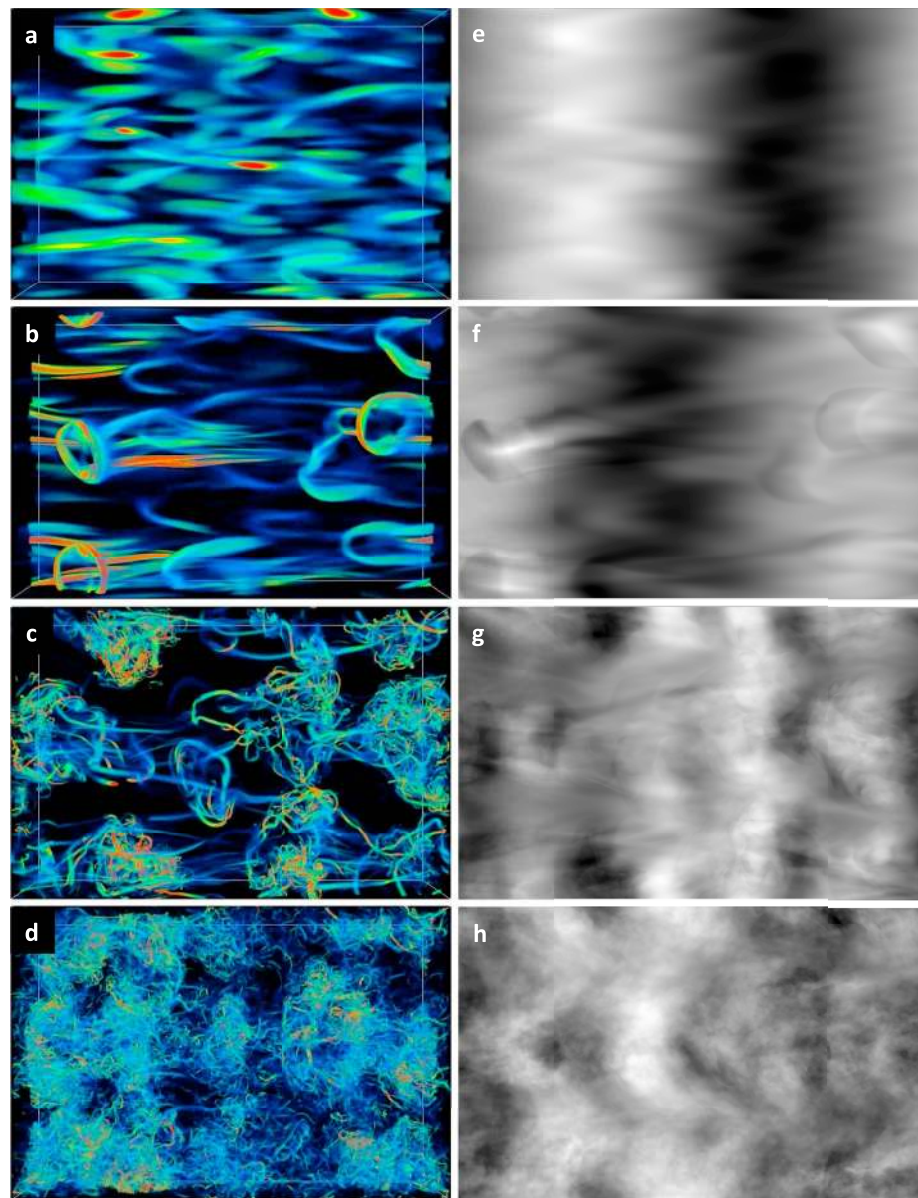
Figure 5. As in Figure 4 for $a = 1.1$ and $\omega_i = N/3.2$ at 9.2, 10.2, 11.2, and 12.2 T_b.

Multiscale DNS yield additional instability dynamics and an expectation for different instability types and/or scales at different locations within the larger-scale flow (Fritts et al., 2013, 2017). Such superpositions are likely present in this event, and we should expect their large amplitudes and high frequencies to favor GW breaking, and perhaps accompanying KHI, as a result.

4.1. Instability Event 1 (IE1): MW Breaking

Increasing MW amplitudes prior to 11 UT yield initial indications of flow instabilities at several sites. The site that exhibits the clearest early instability signatures is the sharp E-W gradient in T at ~35–45 km N of the image center near 11 UT (see the rectangles in Figures 1a and 1e). The instability evolution is shown in Figure 9 with images of OH I for FOVs of ~32 × 54 km from 11:00 to 11:22 UT. Note that for this and subsequent instability events, we show portions of the original images, rather than geographically mapped images, in order to preserve the best resolution. We also note that the AMTM intensity images were obtained using a 10-s integration in order to ensure high spatial resolution of the evolving MW and instability fields.
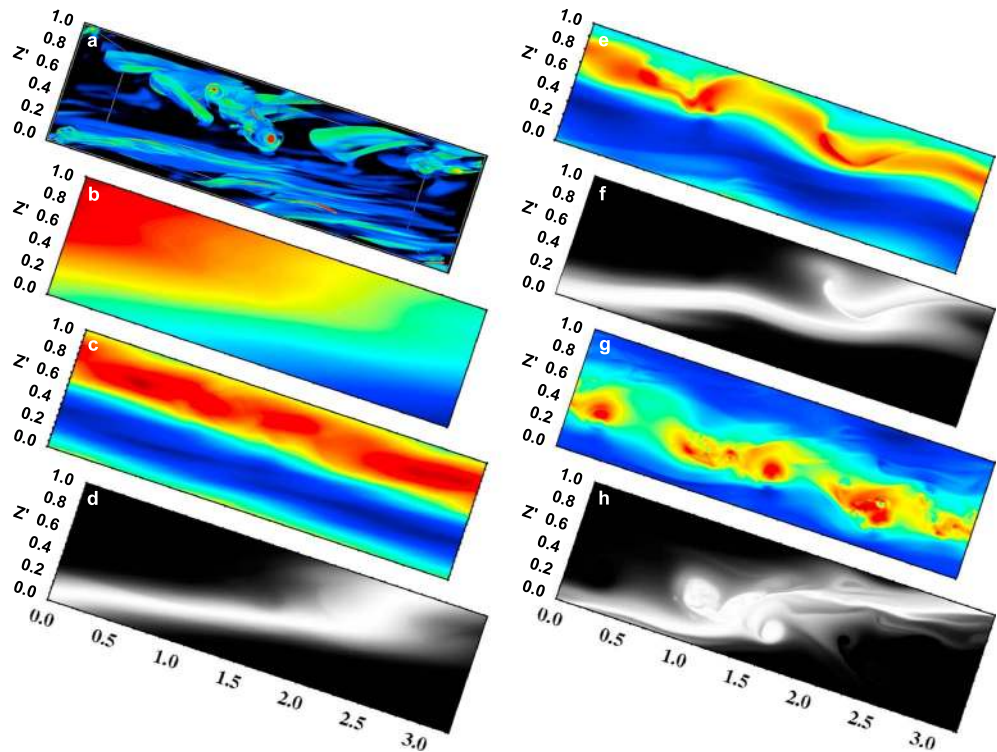
Figure 6. (a) Streamwise-vertical (x,z) cross sections of 3-D vortex structures and (b–d) spanwise-mean T, u, and I for GW breaking DNS with $a = 0.9$ and $\omega_i = N/3.2$ at 22 T_b, corresponding to Figure 4b. (e, g) (x,z) cross sections of T' and (f, h) I' at 22 and 23 T_b, respectively.

The image at 11 UT reveals staggered brighter and darker NE-SW features at N-S scales ~5 km in the upper-central portion of the white oval. It also reveals weaker small-scale bands spaced at ~3 km to the SW that are nearly normal to an extended dark (cold) phase (see the lower region within the oval in Figure 9a). The larger-scale features intensify rapidly and closely resemble those seen in the right panels of Figure 5, especially the paired features to the NE of the bright star in Figure 9c, and have largely abated by 11:08 UT.

The bands expand to the north, advect to the SE, and contribute to variations of the bright MW phase that evolves clear cusp-like structures comprising bright-dark E-W pairs, staggered by ~2–3 km N-S. These appear to be replacing the larger-scale features just discussed at 11:05 and to survive until ~11:10 (Figure 9e). These are followed by new, larger-scale features and successive smaller-scale features decaying by ~11:14, another repetition of this sequence extending from ~11:16–11:20, and a third emerging again at 11:20.

The overall evolution spanning these times indicates a succession of individual instability events having the following features:

1. several event scales (initially ~4–5 km, then ~2–3 km along the MW phase) that arise at common phases of the large-scale MW;
2. progression together towards SE along the larger-scale MW phase at ~30 ms^{-1}, and
3. significant variations in event scales (from larger to smaller within each) that suggest a progression from deeper to shallower instability depths or different contributing MW λ_z.

Of the modeled instability forms discussed above, the one suggested by the observed evolution is the progression from initial counter-rotating vortices, to vortex rings, and their breakdown to turbulence accompanying MW breaking spanning ~2 T_b or less. Specifically, the initial bands seen at 11:00 UT suggest elongated, approximately shear-aligned, successive vortex pairs that induce AMTM T and I enhancements that are weak due to relatively shallow instability dynamics in a deeper OH layer. The attainment thereafter of successive organized structures of staggered dark-bright features suggests coherent vortex rings as predicted by F09b and observed in PMC images by Miller et al. (2015) and Fritts et al. (2017) and to be discussed further
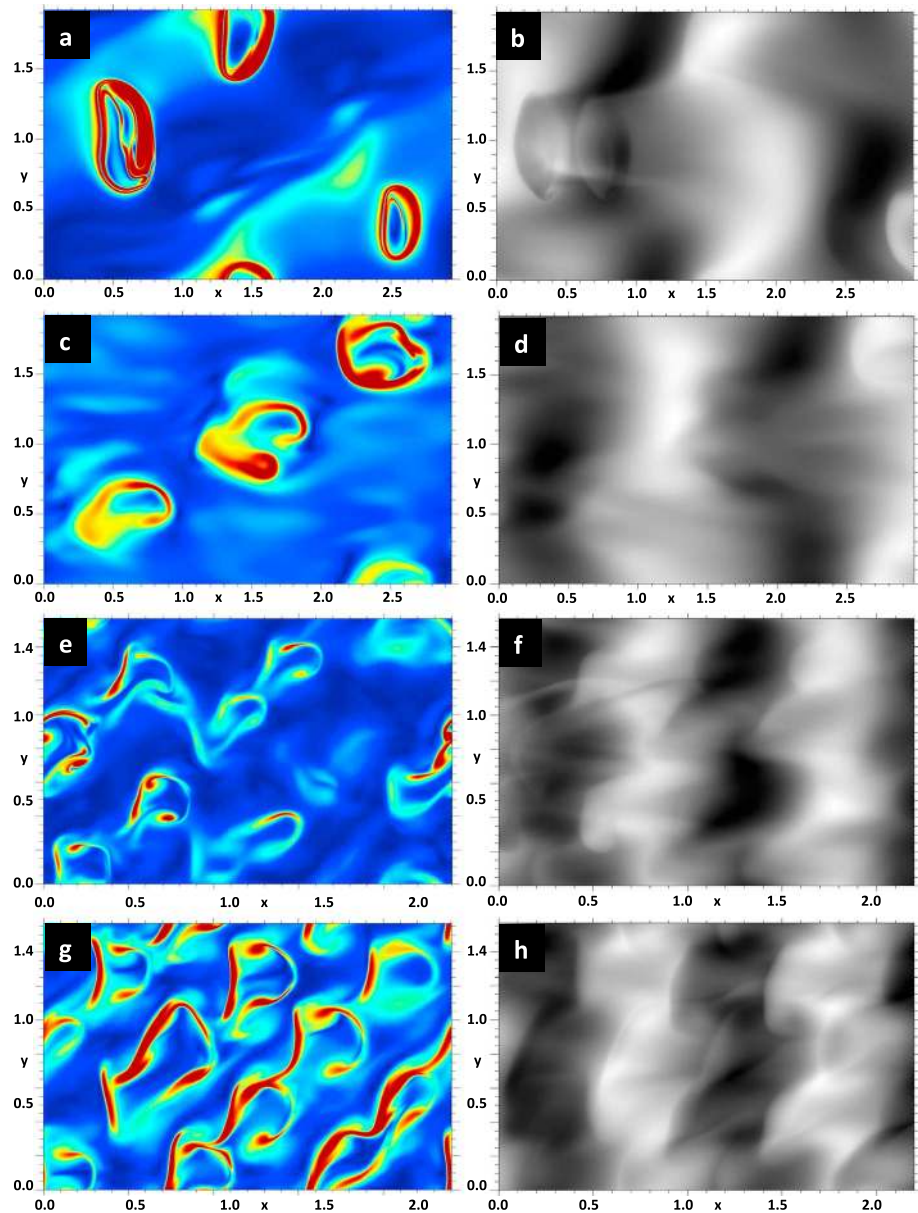
Figure 7. (left) As in Figure 4, but for (x', y') cross sections of vorticity magnitude at one altitude and (right) simulated OH airglow brightness at the times of peak vortex loop or ring coherence for (a and b) $a = 0.9$ and $\omega_i = N/2$, (c and d) $a = 1.1$ and $\omega_i = N/2$, (e and f) $a = 0.9$ and $\omega_i = N/1.4$, and (g and h) $a = 1.1$ and $\omega_i = N/1.4$. Note the different domain dimensions for $\omega_i = N/2$ and $N/1.4$.

below. The apparent evolution and breakdown of these structures, in successive events at the same site with similar scales and geometries, span >22 min (>4 T_b) and are consistent with the individual event evolution time scales predicted by F09b.

The I fields for GW breaking at $\omega_i = N/3.2$ in Figures 4 and 5 show the major dark regions in vertically integrated I to occur ahead of (or within) the vortex rings following their formation in all cases (to the left or westward for westward MW propagation). They also persist into the turbulent decay phase of the vortex rings and thus have clear $I(x,y)$ signatures that survive for short times thereafter. Similar responses are seen for $\omega_i = N/2$ and $N/1.4$ (Figure 7), though with increasing complexity as ω_i and a increase. These fields also exhibit closer spacings of vortex features and their I responses (streamwise and spanwise—note the smaller axis scales with increasing ω_i relative to those in Figures 4 and 5) and more rapid evolutions to turbulence
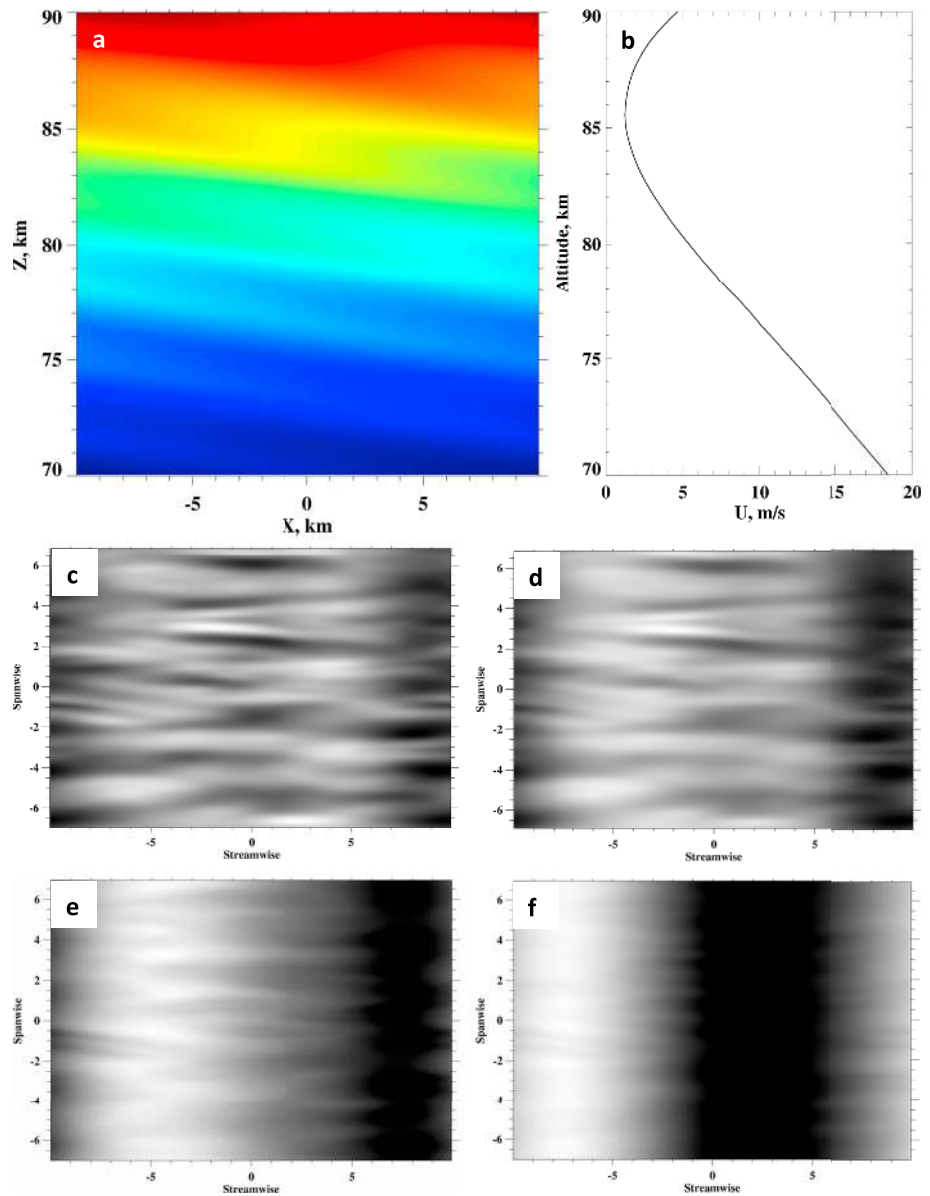
Figure 8. (a) $\theta(x,z)$, (b) $U(z)$, and (c–f) computed $I(x,y)$ at altitudes of $z_{OH} = 70$, 73, 77, and 80 km at one time in a generic anelastic numerical simulation of a GW propagating in a GW-induced mean wind shear. The $I(x,y)$ fields reveal that initial instability character varies with altitude, yielding smaller spanwise scales as λ_z decreases with decreasing $\omega_i = k(c - U)$.

(not shown). The implications are that hydrostatic and nonhydrostatic MWs will exhibit significantly different instability dynamics and OH I responses for the same MW λ_z. Hence, we should expect the instability character in a superposed MW field to depend on which MW components and which MW phases and λ_z dictate the instability responses at a specific time and location.

Referring to the discussion above, we note that the $I(x,y)$ evolution displayed in Figure 9 exhibits alternating larger-scale and smaller-scale instability responses that are indicative of hydrostatic and nonhydrostatic MW instability dynamics at different stages throughout IE1. Specifically, there are apparently portions of four successive and/or overlapping vortex ring formation and breakdown events throughout the evolution shown in Figure 9. Larger-scale features exhibiting vortex ring signatures similar to those seen in Figures 4c and 4g are seen in Figures 9a–9c, 9f, 9g, and beginning in Figure 9l. Similar staggered smaller-scale features are most apparent in the images in Figures 9d, 9e, and 9h–9k. Importantly perhaps, the occurrences of the smaller-scale features appear to accompany, and immediately follow,
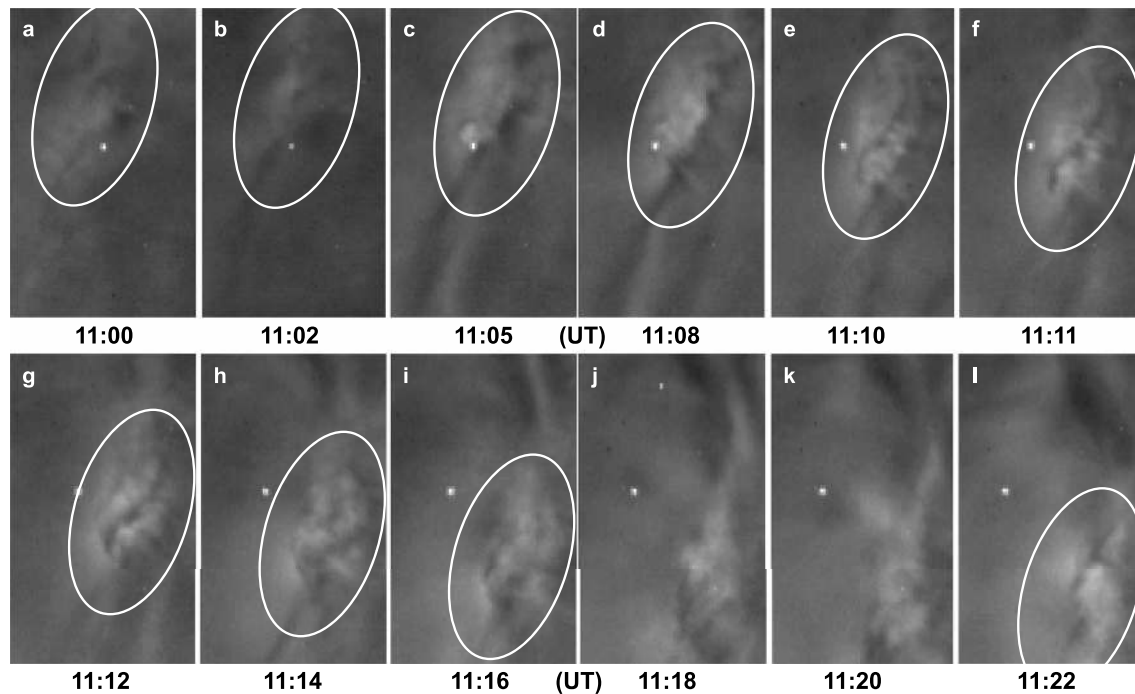
Figure 9. Instability event 1 (IE1) in a ~32 × 54-km subdomain (see Figures 1a and 1e) showing the evolutions of apparent successive vortex rings at large and smaller scales spanning ~2 T_b. The OH layer in this case highlights instability character at the lower edge of the unstable MW phase near the transition from the warmest to the coldest MW phase from west to east because z_{OH} during IE1 is below the maximum MW T' seen by the lidar at Lauder (see Figure 2c). Seen in each case is evidence of staggered instability structures in the spanwise direction.

the presence of more intense, smaller-scale (λ_x ~10–15 km) MWs with phases extending N-S through this region in Figures 9c, 9d, and 9h–9k (see the I variations north and south of the primary MW instabilities).

We now consider the implications of the instability dynamics scales for an independent assessment of the MW λ_z and consistency with our modeling. As noted in the discussion of Figure 7, instability scales depend strongly on the GW ω_i and a when the GW is nonhydrostatic. In contrast, the results in Figures 4 and 5 for more nearly hydrostatic GWs suggest that the spanwise spacing between adjacent vortex ring rows is ~λ_z or somewhat larger. A hydrostatic GW period is comparable to or larger than the interval displayed in Figure 9. Within this interval, the largest vortex ring spacing is thus likely the best conservative (low) estimate of the likely MW λ_z driving these instabilities. This scale is ~7 km from Figures 9c and 9l, implying a minimum λ_z ~8 km. Referring to the lidar $T(z)$ in Figure 2, we see that λ_z decreased from ~14 to ~11 km from 11 to 11:30 UT during this event.

Alternatively, if the λ_x ~10–15 km MW played a significant role in initiating these instability dynamics, as might be argued based on their strong localization in the zonal direction, then the $\omega_i = N/1.4$ case might be more representative when very small instability scales are seen. In this case, the smaller vortex spacings of ~2–3 km suggest instabilities within a MW having λ_z ~10–12 km that appears to agree well with those seen in the lidar $T(z)$ profiles at these times.

The implications of the AMTM observations of apparently alternating, or potentially superposed, larger- and smaller-scale instability dynamics seen in Figure 9 are that instability seeding likely depends strongly on the local environment and that this can change rapidly on the timescales implied by the superposed and non-linear MW dynamics at the inferred range of ω_i.

4.2. Instability Event 2 (IE2): Multiscale MW Breaking

An apparent continuation of the instability dynamics described in IE1 is seen to have extended over a larger region south and east of the location of IE1. These dynamics are shown with I images in an ~43 × 110-
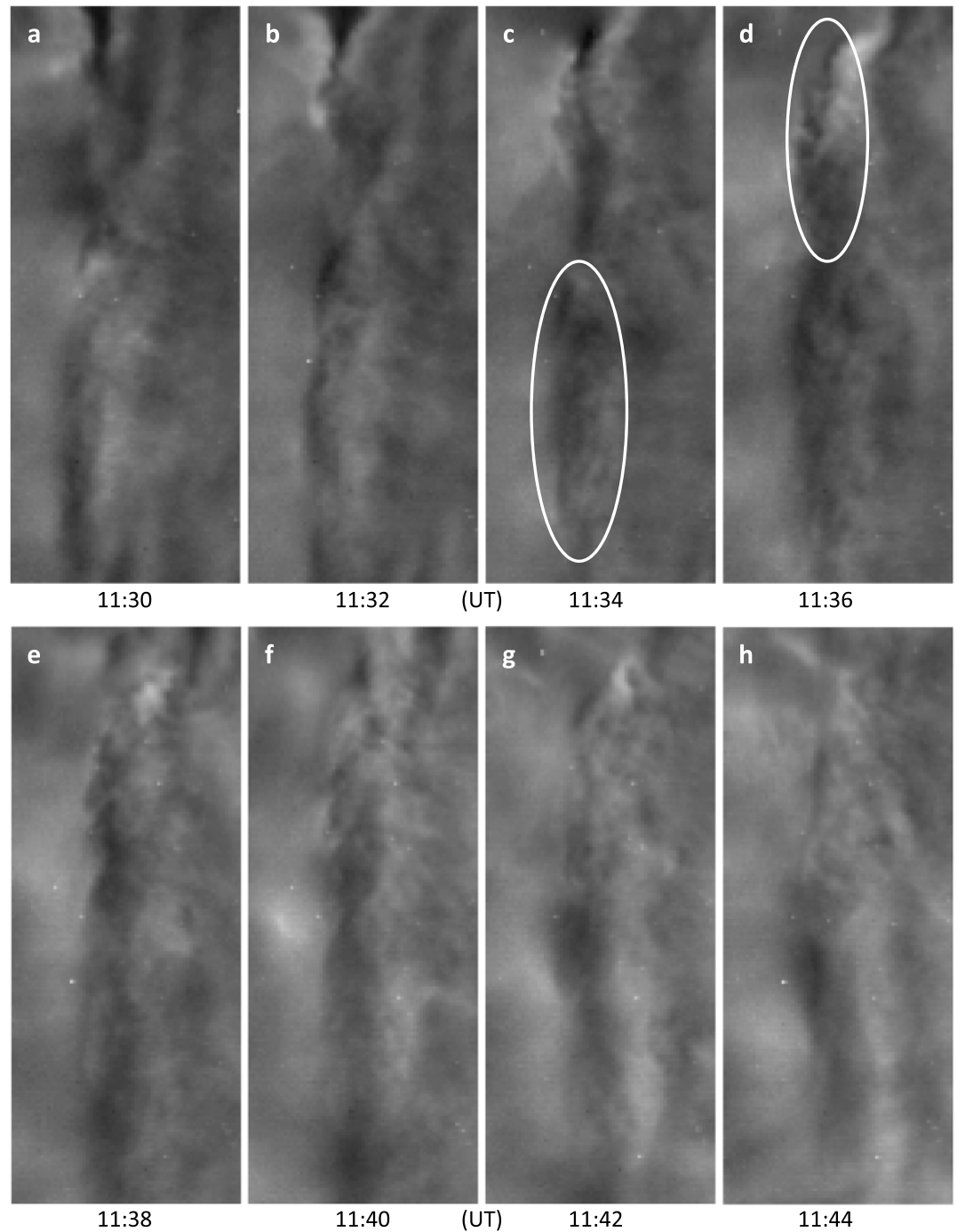
Figure 10. As in Figure 9 for IE2 in the ~43 × 110-km subdomain shown in Figures 1b and 1f. IE2 instability features occur primarily in the lee (east) of the large-scale MW warm phase at left in these images accompanying the warm phase of the superposed λ_x~20-km MW.

km FOV (see the rectangles in Figures 1b and 1f) from 11:30 to 11:44 UT in Figure 10. The bright phase at left in each image is the superposed MW phase at which the IE1 instabilities occurred. In this case, smaller-scale instabilities were by far the dominant features. These largely arose in the trailing bright (warm) phase (to the right) of the λ_x~20-km MW at center and center-right of the images in Figure 10. Referring to Figures 1 and 2, we see that the instability environment was significantly cooler than in IE1 and that dT/dz was superadiabatic above the T' maximum somewhat below (note that the lidar

beam was near the left center of the images in Figure 10, hence measured a lower and warmer large-scale MW phase than accompanied IE2).

As in IE1, the image sequence in Figure 10 reveals multiple sites of instability formation and decay that have similar character to those discussed above. Those at the north end of the FOV achieved strong coherent vortex ring structures by ~11:36 UT (see oval in Figure 9d) and decayed slowly thereafter. Those at the center and S end of the FOV exhibited strong growth to 11:34 UT (see oval in Figure 9c), diminished by ~11:36–11:38 UT, reformed again more weakly by ~11:40 UT, and dissipated thereafter. In all of these instability locations, they appeared to exhibit the staggered bright and dark cusp-like patterns and evolution time scales that were anticipated by our DNS results in Figures 4–7.

The smaller instability scales, like those in IE1, and the dominance of the AMTM $T(x,y)$ variations by the λ_x~20-km MW suggest a largely nonhydrostatic environment in this case. Noting that the lidar λ_z near 82 km at 11:30 UT was ~10 km, this suggests an effective ω_i ~$N/2$ for the λ_x~20-km MW, which is consistent with the smaller instability scales relative to λ_z. The instability locations in IE2 also suggest influences of superposed larger- and smaller-scale MWs. However, we have not yet performed numerical simulations of GW breaking for such cases.

4.3. Instability Event 3 (IE3): Large-Scale Streamwise Instabilities and Vortex Rings

The earlier evolution of the 21 June MW event exhibited primarily smaller-scale instabilities that manifested as vortex loops and rings expected to accompany GW breaking in unsheared or weakly sheared mean flows. Beginning near 12 UT, however, the dominant apparent instabilities exhibited larger-scale initial spanwise variations in T and I: see, for example, the top center of the images in Figures 1c and 1g and the more extensive structures in Figures 1d and 1h at 12:40 UT.

Such streamwise-aligned instability structures were seen to arise in both sheared and unsheared flows as precursors to vortex loops and rings that drive the transition to turbulence in the discussions of Figures 4–8. Hence, we expect that these would also have been seen in IE1 and IE2 above if the OH layer had been at an altitude providing sensitivity to these features. Referring to the lidar $T(z)$ profiles in Figure 2, we see that the nearly adiabatic or superadiabatic layer expected to have accounted for instability dynamics moved down ~2 km from 11 to 12 UT. This moved the major OH sensitivity from a stable (large N) environment below the local T maximum (with sensitivity to the bottom of the unstable layer) into the unstable layer, thus providing sensitivity to both initial streamwise-aligned instabilities at higher altitudes and vortex loop and ring dynamics below (e.g., see Figure 6a and note that the structures are periodic in the vertical).

Figure 11 shows a sequence of I images in the subdomain having dimensions of ~110 × 72 km labeled IE3 in Figures 1c and 1g. The images extend from 11:54 to 12:10 UT, or approximately 3 T_b, at the time when larger-scale, streamwise-aligned apparent instability features were first seen. The image sequence reveals the evolution of initial small-amplitude features (Figure 11a top, right of center) having spanwise scales of ~5–10 km aligned nearly E-W approximately normal to the large-scale (λ_x~60 km; see Figure 1c) MW phase structure. These features intensify, expand to the south, and advect to the ESE from ~11:54 to 12:00 UT. They begin to exhibit significant spanwise modulations along their axes at ~11:58 UT and initiate apparent vortex loops and rings in the warmer instability phases at ~12:00 UT that become more structured and complex prior to dissipating after ~12:06 UT.

Comparing this evolution with the GW breaking dynamics for ω_i~$N/3.2$ shown in Figures 4 and 5 and GW breaking in a mean shear (Figure 8) reveals significant similarities in the observed and predicted features and time scales. The spanwise scales of the brighter features are most similar to those seen in Figures 4a and 4b, though the $I(x,y)$ image in Figure 4e was for an OH brightness z_{OH} below the streamwise-aligned vortices and at a somewhat later time. In particular, the larger feature spacing of ~10 km over the majority of the instability field is nearly the same as the MW λ_z at this time (see Figure 2). This suggests a MW amplitude $a < 1$ and a slower evolution that is consistent with the timescales seen in Figure 11. The spanwise modulations of the instability features in Figures 11b and 10c also bear a close resemblance to the undulations predicted in a sheared environment shown in Figure 8 at the lower altitudes. As noted in the discussion of Figures 4 and 5, these undulations are the precursors of subsequent vortex loops and rings in both unsheared and sheared environments. Finally, the scales of the vortex loop and ring structures of ~4–5 km emerging in
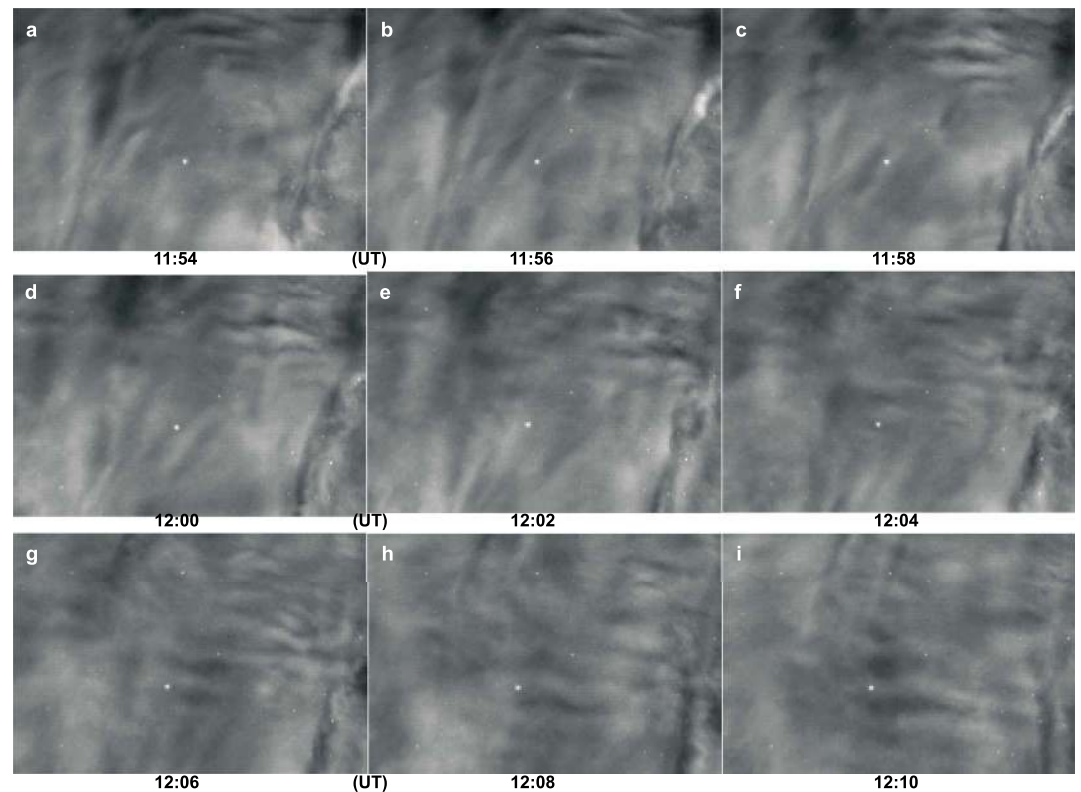
Figure 11. As in Figure 9 for IE3 in the ~110 × 72-km subdomain shown with a solid rectangle in Figures 1c and 1g. IE3 instability features are very different (and more general) than seen in IE1 and IE2. This is due to the lower MW unstable layer at this time seen by the lidar at Lauder ~40 km to the SSE in Figure 2. The lower layer provides continued sensitivity to vortex loops and rings at lower altitudes and new sensitivity to altitudes near and above 87 km at which initial streamwise-aligned instabilities likely rise, based on guidance by our numerical modeling.

Figures 11d–11f also suggest a MW λ_z~10 km, in agreement with that implied by the initial spanwise instability scales and as seen in the lidar $T'(z)$ at these times.

4.4. Instability Events 4 (IE4): Large-Scale Streamwise Instabilities and Breakdown

IE4 is a continuation of IE3 spanning an additional 16 min shown in an ~92 × 92-km subdomain centered slightly to the SE. As in IE3, IE4 features seen in the image center at 12:10 UT (Figure 12a) are relatively uniform along the MW direction of propagation; those to the N have the same orientation but are much weaker at this time. The further evolutions of these fields show that both sets of initial instabilities succumb to strong N-S displacements due to their mutual interactions and that both exhibit a strong breakdown and destruction of the coherent streamwise-aligned features but at somewhat different times. The features initially in the center of the subdomain break down strongly from 12:16 to 12:20 UT; those initially at the top break down strongly from 12:22 to 12:26 UT.

Interestingly, IE4 does not exhibit the evolution from streamwise-aligned vortices to vortex loops and rings seen in IE3. This is likely due to the continued downward motion of the unstable MW layer at which the instabilities arise (see Figure 2c). As noted above, initial streamwise-aligned instabilities accompanying GW breaking occur above the vortex rings that are driven by their mutual interactions (see F09b and Fritts et al., 2017). Thus, an OH layer that highlights vortex dynamics at a constant altitude in a descending GW phase structure would effectively sample vortex rings first, both streamwise-aligned vortices and vortex rings together later and ultimately only the initial streamwise-aligned vortices followed by turbulence at the upper edge of the GW breaking region. This appears to be the progression of instability dynamics due to MW breaking that was observed by the AMTM spanning IE1 to IE4 in the most unstable phase of a MW field that descended ~3 km over 2.5 hr.
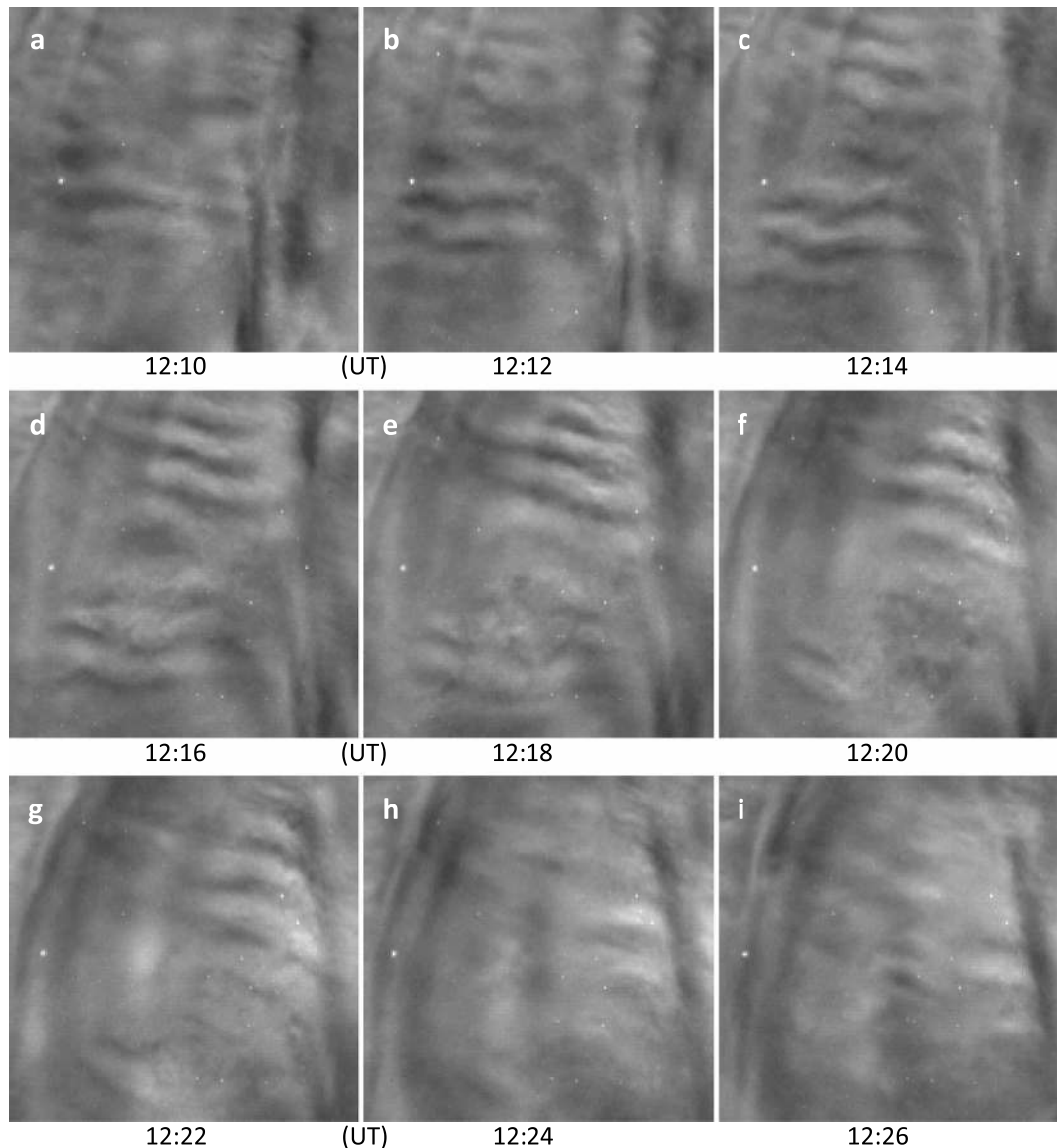
Figure 12. As in Figure 9 for IE4 in the ~92 × 92-km subdomain shown with a dashed rectangle in Figures 1c and 1g. The dominant responses in IE4 include streamwise-aligned instabilities, their mutual interactions and breakdown, and apparent large-scale turbulence extending from ~12:16–12:22 UT. The further progression of the unstable MW phase to lower altitudes (see Figure 2c) prior to IE4 appears to yield additional sensitivity to instability dynamics and responses higher within the unstable layer and lack of sensitivity to vortex ring dynamics in this case.

4.5. Instability Event 5 (IE5): Small-Scale Streamwise Vortices

Both larger- and smaller-scale instability structures are seen at a later stage in the MW breaking evolution shown in Figure 13. The FOV here is ~90 × 145 km (see subdomain IE5 in Figures 1d and 1h) and the evolution spans ~2 T_b. As noted in the discussion of the MW field evolution in section 3, the zonal mean wind was likely decreasing with altitude and time during this later instability event (see Figure 3), and the MW amplitude over most of the AMTM FOV was much smaller than at earlier times. $I(x,y)$ images revealed a dominant MW having λ_x~40–60 km and a phase aligned roughly N-S. Smaller λ_x MWs also contributed to the $I(x,y)$ variations but appeared to play smaller roles than in IE1 and IE2. The lidar $T(z)$ at these times revealed a significant reduction in the MW amplitude, a decreasing negative large-scale dT/dz at these altitudes, and the evolution of apparently relatively stable layering in the $T(z)$ profiles at smaller vertical scales accompanying the stabilization of the former superadiabatic layer.
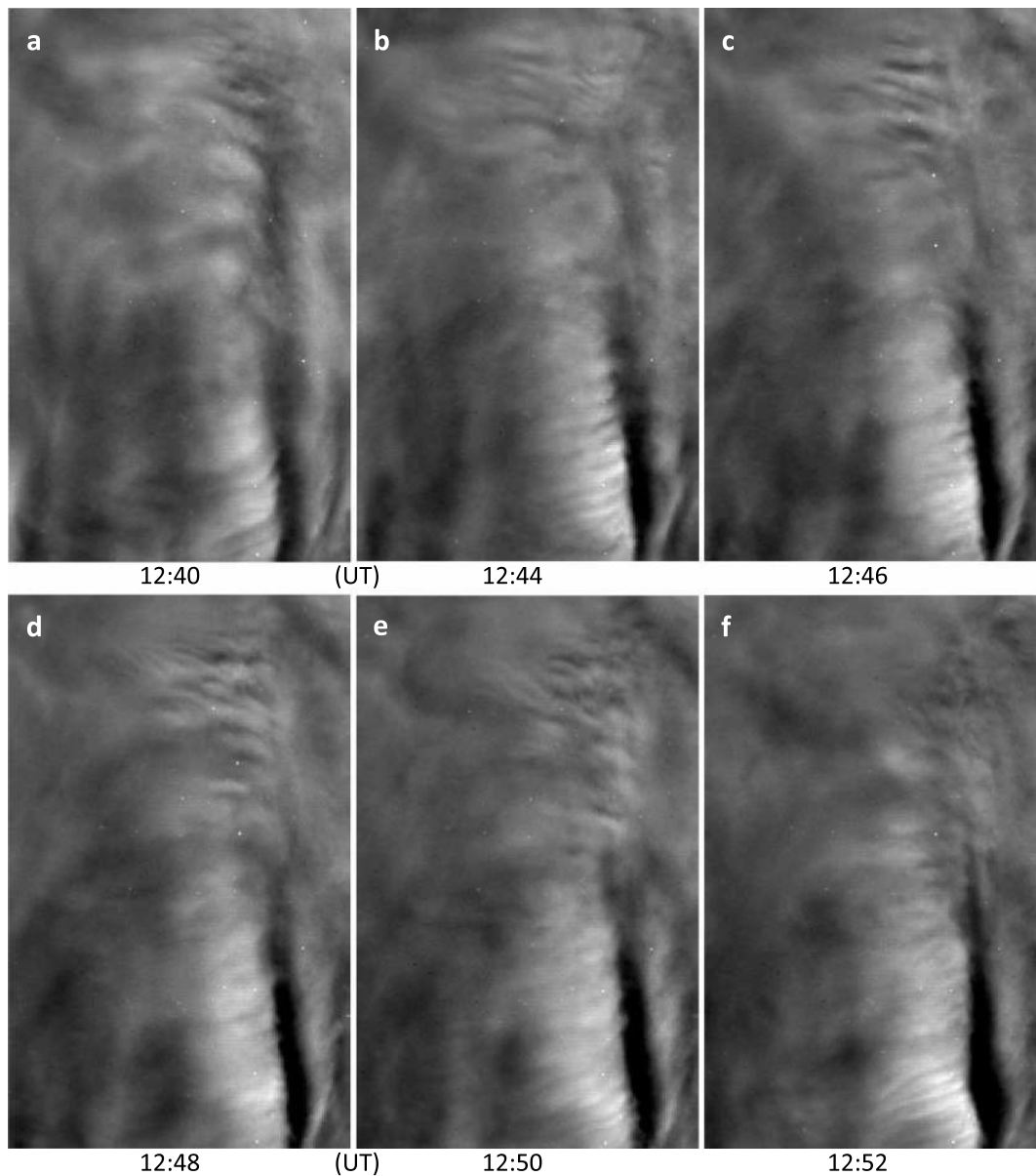
Figure 13. As in Figure 9 for IE5 in the ~90 × 145-km subdomain shown in Figures 1d and 1h. Instability dynamics in IE5 are quite different from those seen above and appear to be strongly influenced by increasing dU/dz accompanying MW momentum deposition and weakening U at higher altitudes. These exhibit both larger- and smaller-scale spanwise I variations at the brightest (warmest) phase of the λ_x~60-km MW, with weak modulation by smaller λ_x MWs.

Importantly, however, the lidar observations were ~70-km NW of the strong overturning MW occurring in the lower-right portion of subdomain IE5 and, thus, may not have been representative of the environment in this region at these times. This MW feature evolved through the migration and merging of the two MW warm-to-cold phase transitions seen at 12 UT at lower right in Figures 1c and 1g (see the AMTM_I.mp4 animation noted above). These dynamics also intensified after 12:40 UT, achieving a maximum AMTM ΔT between the warmest and coldest phases of ~45 K, with the true ΔT likely ~20% larger due to averaging of the brightness-weighted T over the airglow layer, implying a MW amplitude well above $a = 1$.

Instabilities at these times had somewhat different character in the N and S portions of the IE5 sub-domain. Those to the N accompanied a smaller, but significant, MW amplitude and were very similar to those described in IE3 above. Those to the south accompanied a large MW amplitude and were confined to the single, strong warm phase (bright I in Figure 13) and its transition to the cold phase in the overturning

region to the E and above. The latter instabilities exhibited streamwise-aligned features that intensified and decayed from 12:40 to 12:48 UT and intensified again by 12:52 UT. They also exhibited larger and smaller spanwise scales at different times and strong advection towards E and upward into the overturning region of the MW (see the animations). Finally, the spanwise instability scales were larger initially (Figures 13a–13d) and smallest in Figure 13f, suggesting either (1) a change in sensitivity of the AMTM from lower to higher altitudes with time or (2) a descending shear layer imposing smaller $\omega_i = k(c - U)$ and smaller implied spanwise instability scales at later times (see Figures 8c–8f); see, for example, the continuing descent of the maximum T' above 80 km from 12 to 13 UT in Figure 2. There is no indication in these images of subsequent vortex rings, though they also occur in the DNS with mean shear shown in Figure 8 at later times. This suggests an earlier stage of MW instability in Figure 13.

5. Discussion

Many previous observational studies have suggested possible GW breaking in the MLT, but relatively few have directly observed specific instability dynamics and their environments. Superadiabatic lapse rates in the stratosphere and MLT were observed by rocket grenade, pitot tube, falling sphere, and other techniques beginning in the 1960s (Fritts et al., 1988; Goldberg et al., 2006; Hodges, 1969; Theon et al., 1967). More recently, ionization gauges have extended MLT profiling capabilities to include turbulence assessments, providing more direct indications of instabilities and enabling correlations among these fields (Lehmacher et al., 2011; Lübken, 1997; Lübken et al., 2002; Rapp et al., 2004; Strelnikov et al., 2009; Szewczyk et al., 2013). Likewise, ground-based and/or airborne lidars have observed overturning in Na densities and mixing ratios, superadiabatic gradients, and their environments over significant depths (Bossert et al., 2017; Fritts et al., 2004; Hecht, 2004; Hecht et al., 2005; Larsen et al., 2004; Liu et al., 2004; Williams et al., 2006).

Other studies employing airglow, AMTM OH $T(x,y)$, and NLC imaging have yielded more direct evidence of GW breaking leading to instabilities and turbulence at multiple locations. These have provided key information on GW and instability spatial and temporal scales and the relations among them, but often without characterization of the local environment. Examples include OH imager observations of instabilities and breakdown of GWs (Hecht et al., 1997, 2018; Yamada et al., 2001) and high-resolution imaging of GW instability dynamics and turbulence seen in NLC displays in polar summer (Fritts et al., 1993, 2017; Miller et al., 2015; Witt, 1962). These studies suggest that GWs contributing most to strong wave breaking and turbulence in the MLT (i.e., those accounting for the major energy fluxes and deposition and the deeper superadiabatic layers) are those having λ_z~5–20 km and $\omega_i > N/10$ (hence, λ_h~200 km or less). Where specific instability character has been inferred, the more recognizable forms include those anticipated by various modeling studies, specifically initial optimal perturbations leading to streamwise-aligned instabilities at finite amplitude, vortex loops and rings that arise in response, and apparent intrusions in multiscale flows (see Achatz, 2005, 2007; F09a; Fritts et al., 2013, 2017; Hecht et al., 2018). Of these, only the ground-based NLC observations analyzed by Fritts et al. (2017) have revealed a link between initial streamwise-aligned instabilities and the vortex rings that drive the transition to turbulence to date. Airglow and NLC imaging have also revealed multiple instances of KHI arising due to wind shear and stability profiles contributed, in part, by apparent GWs at lower and higher intrinsic frequencies (Baumgarten & Fritts, 2014; Fritts et al., 2018; Hecht et al., 2014), though these dynamics are not relevant to the observations discussed in this paper.

More recent studies addressing MLT "ship-wave" responses observed over the Auckland Islands using DEEPWAVE airborne AMTM and Na lidar measurements were performed by Eckermann et al. (2016), Pautet et al. (2016), and Broutman et al. (2017). These studies did not model nonlinear instability dynamics, focusing instead on the 3-D observed (or linear) dynamics of this MW event spanning four overflights and the transition to incipient wave breaking at ~78-km altitude. However, AMTM images reveal apparent instabilities and large-scale turbulence due to large ship-wave amplitudes and breaking, both in the lee of Auckland Islands and to the north and south spanning ~4 hr. AMTM and Na lidar measurements coupled with ray modeling revealed a 3-D ship-wave response in the MLT having λ_h~40 km, λ_z~20 km or larger, and an amplitude a ~1 (Eckermann et al., 2016). AMTM imaging also revealed apparent vortex ring signatures having diameters of ~5km or larger at different locations in the response on successive overflights and MW phases, implying a λ_z~10 km or larger that is consistent with AMTM temperature and Na lidar Na

density measurements and ray tracing. Not captured in these data, however, were the temporal evolutions of the instability events, including the precursors of vortex rings, since successive overflights were separated by 40 min or more.

Results presented here include high-resolution measurements, in space and time, of MW and instability structures that are captured due to the AMTM sensitivity to different MW phases for multiple events exhibiting varying MW intrinsic properties. Instability events 1–4 (IE1–4) provide direct evidence of vortex loops and rings as the dominant pathway to turbulence, their spatial and temporal scales, and the relations of their scales to those of the breaking MWs. IE3–5 provide evidence of the formation and evolution of initial streamwise-aligned instabilities, their relations to the underlying MW character, and their mutual interactions driving vortex loop and ring formation. Rayleigh lidar measurements enable the relation of MW instability features to specific MW phases, specifically the evolution of initial and finite-amplitude instabilities in the most unstable phases of the MWs, and the occurrence of initial streamwise-aligned instabilities above the resulting vortex loops and rings.

Comparisons of these observations with DNS of GW breaking and instability dynamics for various GW amplitudes, frequencies, and environments appear to confirm model predictions in several areas. These include the dominant instability pathways accompanying idealized GW breaking, the time scales for the instability evolutions and breakdown to turbulence, and the relations among the GW and instability scales for both unsheared and sheared mean flows.

Finally, there are several other interesting implications of our data analysis presented above. GW breaking must impact the GW amplitude at higher altitudes, and local mean flow accelerations in the direction of GW propagation must accompany GW momentum flux divergence. Observations of successive nearly adiabatic or superadiabatic layers seen in many MLT temperature profiles noted above, and our numerical modeling, suggest that GW breaking limits a GW amplitude but allows it to continue to propagate vertically. Our lidar observations of superadiabatic layers at successive GW phases in the vertical provide strong support for this expectation in a case where a MW dominated the MLT GW field. Specifically, expected instability dynamics occurring at lower superadiabatic layers (not seen by the AMTM, but implied by Rayleigh lidar measurements in Figure 2b) did not prevent the large-amplitude MW from exhibiting instabilities in the OH layer above, as also noted by Bramberger et al. (2017) and Fritts et al. (2018) for other DEEPWAVE events.

Similarly, MW momentum deposition at the altitude of strong instability dynamics during the 21 June event implies strong local zonal wind decelerations, though these are advected downstream thereafter. Sustained GW breaking and momentum deposition will nevertheless yield local decelerations, reduced mean zonal winds, increased westward shear (more negative dU/dz) below, and reduced MW λ_z. Our lidar measurements reveal that the MW λ_z decreases strongly from ~20 km at 9:30 UT to ~14 km at 11 UT to ~10 km at ~12 UT following strong MW breaking. This suggests a reduction of U to ~20 ms^{-1} in the wave breaking region, and even weaker winds above, assuming a mean $dT/dz \sim -3$ Kkm^{-1}, $N \sim 0.018$ s^{-1} as above (also see Figure 2 profiles at later times), and approximately hydrostatic MWs.

Finally, the occurrences of stronger instability dynamics discussed above appear to correlate with the temporal variability of peak MW MFs discussed by T19. Specifically, the strong instabilities seen in IE1 centered near ~11:10 UT, extending from ~11:30 to 11:40 UT in IE2, and beginning prior to 12 UT in IE3 and IE4 exhibit clear correlations with those times seen by T19 to experience minima or decreasing MFs assessed in that paper.

6. Summary and Conclusions

We have analyzed five instability events accompanying MW breaking observed on 21 June 2014 as part of the DEEPWAVE measurement program. A ground-based AMTM and Rayleigh lidar at Lauder on NZ SI enabled continuous imaging of $T(x,y)$ and profiling of $T(z)$ and $T'(z)$ in the center of the AMTM FOV spanning many hours. These measurements allowed simultaneous and coincident quantification of the following:

1. MW scales, orientations, and amplitudes, including overturning, in the mesosphere,
2. evolution of $T(z)$ and $T'(z)$ throughout the MW breaking and instability events,
3. locations of instabilities within the MW field and correlations with overturning regions, and
4. instability evolutions from initial perturbations to large amplitudes and MW breakdown.

Our event analyses were aided by numerical simulations of multiple GW breaking events for various amplitudes, intrinsic frequencies, and environments (e.g., overturning and statically stable MWs, and both unsheared and sheared mean flows). Comparisons of our measurements and modeling confirmed model predictions of the general character and evolutions of instabilities causing GW breakdown in cases where the flows were somewhat idealized. Our results suggest relatively robust pathways to turbulence accompanying GW breaking in large-scale flows that vary slowly in the vertical.

Idealized large-amplitude GW dynamics are not universal, however. More general environments comprising superposed GWs and other motions at multiple spatial and temporal scales enable an expanded spectrum of "multiscale" interactions. These include GW breaking and additional instabilities that exhibit various scales, characteristics, and intensities: for example, local and larger-scale GWs, smaller- and larger-scale KHI, and GW instabilities exhibiting a diversity of forms (Fritts et al., 2013; Fritts et al., 2016, 2017; Fritts, Wan, et al., 2014; Hecht et al., 1997, 2005, 2014, 2018; Miller et al., 2015; Walterscheid et al., 2013). We expect these and other DEEPWAVE observations of small-scale MW and instability dynamics and related observations of similar dynamics to motivate new modeling studies addressing more realistic 3-D environments in the future.

References

Achatz, U. (2005). On the role of optimal perturbations in the instability of monochromatic gravity waves. *Physics of Fluids*, *17*(9), 094107. https://doi.org/10.1063/1.2046709

Achatz, U. (2007). The primary nonlinear dynamics of modal and nonmodal perturbations of monochromatic inertia-gravity waves. *Journal of the Atmospheric Sciences*, *64*(1), 74–95. https://doi.org/10.1175/JAS3827.1

Andreassen, Ø., Hvidsten, P. Ø., Fritts, D. C., & Arendt, S. (1998). Vorticity dynamics in a breaking gravity wave, 1. Initial instability evolution. *Journal of Fluid Mechanics*, *367*, 27–46. https://doi.org/10.1017/S0022112098001645

Baumgarten, G., & Fritts, D. C. (2014). Quantifying Kelvin-Helmholtz instability dynamics observed in noctilucent clouds: 1. Methods and observations. *Journal of Geophysical Research: Atmospheres*, *119*, 9324–9337. https://doi.org/10.1002/2014JD021832

Bossert, K., Fritts, D. C., Heale, C. J., Eckermann, S. D., Plane, J. M. C., Snively, J. B., et al. (2018). Momentum flux spectra of a mountain wave event over New Zealand. *Journal of Geophysical Research: Atmospheres*, *123*, 9980–9991. https://doi.org/10.1029/2018JD028319

Bossert, K., Fritts, D. C., Pautet, P. D., Williams, B. P., Taylor, M. J., Kaifler, B., et al. (2015). Momentum flux estimates accompanying multiscale gravity waves over Mount Cook, New Zealand, on 13 July 2014 during the DEEPWAVE campaign. *Journal of Geophysical Research: Atmospheres*, *120*, 9323–9337. https://doi.org/10.1002/2015JD023197

Bossert, K., Fritts, D. C., Williams, B. P., Pautet, P.-D., & Taylor, M. J. (2017). Secondary gravity wave generation over New Zealand during the DEEPWAVE campaign. *Journal of Geophysical Research: Atmospheres*, *122*, 7834–7850. https://doi.org/10.1002/2016JD026079

Bourget, B., Dauxois, T., Joubaud, S., & Odier, P. (2013). Experimental study of parametric subharmonic instability for internal plane waves. *Journal of Fluid Mechanics*, *723*, 1–20. https://doi.org/10.1017/jfm.2013.78

Bramberger, M., Dörnbrack, A., Bossert, K., Ehard, B., Kaifler, B., Mallaun, C., & Witschas, B. (2017). Does strong tropospheric forcing cause large-amplitude mesospheric gravity waves? A DEEPWAVE case study. *Journal of Geophysical Research: Atmospheres*, *122*, 11,422–11,443. https://doi.org/10.1002/2017JD026 273

Broutman, D., Eckermann, S. D., Knight, H., & Ma, J. (2017). A stationary phase solution for mountain waves with application to mesospheric mountain waves generated by Auckland Island. *Journal of Geophysical Research: Atmospheres*, *122*, 699–711. https://doi.org/10.1002/2016JD025699

Dosser, H. V., & Sutherland, B. R. (2011). Weakly nonlinear non-Boussinesq internal gravity wavepackets. *Physica D*, *240*(3), 346–356. https://doi.org/10.1016/j.physd.2010.09.008

Eaton, F. D., McLaughlin, S. A., & Hines, J. R. (1995). A new frequency modulated continuous wave radar for studying planetary boundary layer morphology. *Radio Science*, *30*(1), 75–88. https://doi.org/10.1029/94RS01937

Eckermann, S. D., Broutman, D., Ma, J., Doyle, J. D., Pautet, P.-D., Taylor, M. J., et al. (2016). Dynamics of orographic gravity waves observed in the mesosphere over the Auckland islands during the Deep Propagating Gravity Wave Experiment (DEEPWAVE). *Journal of the Atmospheric Sciences*, *73*(10), 3855–3876. https://doi.org/10.1175/JAS-D-16-0059.1

Eckermann, S. D., Ma, J., Hoppel, K. W., Kuhl, D. D., Allen, D. R., Doyle, J. A., et al. (2018). High-altitude (0–100 km) global atmospheric reanalysis system: Description and application to the 2014 austral winter of the Deep Propagating Gravity-Wave Experiment (DEEPWAVE). *Monthly Weather Review*, *146*(8), 2639–2666. https://doi.org/10.1175/MWR-D-17-0386.1

Fritts, D. C., & Alexander, M. J. (2003). Gravity dynamics and effects in the middle atmosphere. *Reviews of Geophysics*, *41*(1), 1003. https://doi.org/10.1029/2001RG000106

Fritts, D. C., Baumgarten, G., Wan, K., Werne, J. A., & Lund, T. (2014). Quantifying Kelvin-Helmholtz instability dynamics observed in noctilucent clouds: 2. Modeling and interpretation of observations. *Journal of Geophysical Research: Atmospheres*, *119*, 9324–9337. https://doi.org/10.1002/2014JD021833

Fritts, D. C., Isler, J. R., Thomas, G. E., & Andreassen, Ø. (1993). Wave breaking signatures in noctilucent clouds. *Geophysical Research Letters*, *20*(19), 2039–2042. https://doi.org/10.1029/93GL01982

Fritts, D. C., Laughman, B., Lund, T. S., & Snively, J. B. (2015). Self-acceleration and instability of gravity wave packets: 1. Effects of temporal localization. *Journal of Geophysical Research: Atmospheres*, *120*, 8783–8803. https://doi.org/10.1002/2015JD023363

Fritts, D. C., Miller, A. D., Kjellstrand, C. B., Geach, C., Williams, B. P., Kaifler, B., et al. (2019). PMC turbo: Studying gravity wave and instability dynamics in the summer mesosphere using polar mesospheric cloud imaging and profiling from a stratospheric balloon. *Journal of Geophysical Research: Atmospheres*, *124*, 6423–6443. https://doi.org/10.1029/2019JD030298

Fritts, D. C., Pautet, P.-D., Bossert, K., Taylor, M. J., Williams, B. P., Iimura, H., et al. (2014). Quantifying gravity wave momentum fluxes with Mesosphere Temperature Mappers and correlative instrumentation. *Journal of Geophysical Research: Atmospheres*, *119*, 13,583–13,603. https://doi.org/10.1002/2014JD022150

Fritts, D. C., Smith, R. B., Taylor, M. J., Doyle, J. D., Eckermann, S. D., Dörnbrack, A., et al. (2016). The Deep Propagating Gravity Wave Experiment (DEEPWAVE): An airborne and ground-based exploration of gravity wave propagation and effects from their sources throughout the lower and middle atmosphere. *Bulletin of the American Meteorological Society*, *97*(3), 425–453. https://doi.org/10.1175/BAMS-D-14-00269.1

Fritts, D. C., Smith, S. A., Balsley, B. B., & Philbrick, C. R. (1988). Evidence of Gravity Wave Saturation and Local Turbulence Production in the Summer Mesosphere and Lower Thermosphere During the STATE Experiment. *Journal of Geophysical Research*, *93*(D6), 7015–7025.

Fritts, D. C., Vadas, S. A., & Yamada, Y. (2002). An estimate of strong local gravity wave body forcing based on OH airglow and meteor radar observations. *Geophysical Research Letters*, *29*(10), 1429. https://doi.org/10.1029/2001GL013753

Fritts, D. C., Vosper, S. B., Williams, B. P., Bossert, K., Plane, J. M. C., Taylor, M. J., et al. (2018). Large-amplitude mountain waves in the mesosphere accompanying weak cross-mountain flow during DEEPWAVE Research Flight RF22. *Journal of Geophysical Research: Atmospheres*, *123*, 9992. https://doi.org/10.1029/2017JD028250

Fritts, D. C., Wan, K., Werne, J., Lund, T., & Hecht, J. H. (2014). Modeling influences of Kelvin-Helmholtz instability dynamics on airglow. *Journal of Geophysical Research: Atmospheres*, *119*, 8858–8871. https://doi.org/10.1002/2014JD021737

Fritts, D. C., Wang, L., Baumgarten, G., Miller, A. D., Geller, M. A., Jones, G., et al. (2017). High-resolution observations and modeling of turbulence sources, structures, and intensities in the upper mesosphere. *Journal of Atmospheric and Solar - Terrestrial Physics*, *162*, 57–78. https://doi.org/10.1016/j.jastp.2016.11.006

Fritts, D. C., Wang, L., Werne, J., Lund, T., & Wan, K. (2009a). Gravity wave instability dynamics at high Reynolds numbers, 1: Wave field evolution at large amplitudes and high frequencies. *Journal of the Atmospheric Sciences*, *66*(5), 1126–1148. https://doi.org/10.1175/2008JAS2726.1

Fritts, D. C., Wang, L., Werne, J., Lund, T., & Wan, K. (2009b). Gravity wave instability dynamics at high Reynolds numbers, 2: Turbulence evolution, structure, and anisotropy. *Journal of the Atmospheric Sciences*, *66*(5), 1149–1171. https://doi.org/10.1175/2008JAS2727.1

Fritts, D. C., Wang, L., & Werne, J. A. (2013). Gravity wave-fine structure interactions. Part I: Influences of fine structure form and orientation on flow evolution and instability. *Journal of the Atmospheric Sciences*, *70*(12), 3710–3734. https://doi.org/10.1175/JAS-D-13-055.1

Fritts, D. C., Williams, B. P., She, C.-Y., Vance, J. D., Rapp, M., Lübken, F.-J., et al. (2004). Observations of extreme temperature and wind gradients near the summer mesopause during the MaCWAVE/MIDAS rocket campaign. *Geophysical Research Letters*, *31*, L24S06. https://doi.org/10.1029/2003GL019389

Fruman, M. D., & Achatz, U. (2012). Secondary instabilities in breaking inertia-gravity waves. *Journal of the Atmospheric Sciences*, *69*, 303–322. https://doi.org/10.1175/JAS-D-10-05027.1

Goldberg, R. A., Fritts, D. C., Schmidlin, F. J., Williams, B. P., Croskey, C. L., Mitchell, J. D., et al. (2006). The MaCWAVE program to study gravity wave influences on the polar mesosphere. *Annales de Geophysique*, *24*(4), 1159–1173. https://doi.org/10.5194/angeo-24-1159-2006

Grimshaw, R. (1988). Resonant wave interactions in a stratified shear flow. *Journal of Fluid Mechanics*, *190*, 357–374. https://doi.org/10.1017/S0022112088001351

Heale, C. J., Bossert, K., Snively, J. B., Fritts, D. C., Pautet, P.-D., & Taylor, M. J. (2017). Numerical modeling of a multiscale gravity wave event and its airglow signatures over Mount Cook, New Zealand during the DEEPWAVE campaign. *Journal of Geophysical Research: Atmospheres*, *122*, 846–860. https://doi.org/10.1002/2016JD025700

Hecht, J. H. (2004). Instability layers and airglow imaging. *Reviews of Geophysics*, *42*, RG1001. https://doi.org/10.1029/2003RG000131

Hecht, J. H., Fritts, D. C., Wang, L., Gelinas, L. J., Rudy, R. J., Walterscheid, R. L., et al. (2018). Observations of the breakdown of mountain waves over the Andes Lidar Observatory at Cerro Pachon on July 8/9 2012. *Journal of Geophysical Research: Atmospheres*, *123*, 276–299. https://doi.org/10.1002/2017JD027303

Hecht, J. H., Liu, A. Z., Walterscheid, R. L., & Rudy, R. J. (2005). Maui Mesosphere and lower thermosphere (Maui MALT) observations of the evolution of Kelvin-Helmholtz billows formed near 86 km altitude. *Journal of Geophysical Research*, *110*, D09S10. https://doi.org/10.1029/2003JD003908

Hecht, J. H., Walterscheid, R. L., Fritts, D. C., Isler, J. R., Senft, D. C., Gardner, C. S., & Frank, S. J. (1997). Wave breaking signatures in OH airglow and sodium densities and temperatures 1. Airglow imaging, Na lidar, and MF radar observations. *Journal of Geophysical Research*, *102*(D6), 6655–6668. https://doi.org/10.1029/96JD02619

Hecht, J. H., Wan, K., Gelinas, L. J., Fritts, D. C., Walterscheid, R. L., Franke, S. J., et al. (2014). The lifecycle of instability features measured from the Andes Lidar Observatory over Cerro Pachon on March 24, 2012. *Journal of Geophysical Research: Atmospheres*, *119*, 8872–8898. https://doi.org/10.1002/2014JD021726

Hodges, R. R. Jr. (1969). Eddy diffusion coefficients due to instabilities in internal gravity waves. *Journal of Geophysical Research*, *74*(16), 4087–4090. https://doi.org/10.1029/JA074i016p04087

Kaifler, B., Kaifler, N., Ehard, B., Dörnbrack, A., Rapp, M., & Fritts, D. C. (2015). Influences of source conditions on mountain wave penetration into the stratosphere and mesosphere. *Geophysical Research Letters*, *42*, 9488–9494. https://doi.org/10.1002/2015GL066465

Klostermeyer, J. (1991). Two- and three-dimensional parametric instabilities in finite amplitude internal gravity waves. *Geophysical and Astrophysical Fluid Dynamics*, *61*(1-4), 1–25. https://doi.org/10.1080/03091929108229035

Larsen, M. F., Liu, A. Z., Gardner, C. S., Kelley, M. C., Collins, S., Friedman, J., & Hecht, J. H. (2004). Observations of overturning in the upper atmosphere and lower thermosphere. *Journal of Geophysical Research*, *109*, D02S04. https://doi.org/10.1029/2002JD003067

Lehmacher, G. A., Guo, L., Kudeki, E., Reyes, P. M., Akgiray, A., & Chau, J. L. (2007). High-resolution observations of mesospheric layers with the Jicamarca VHF radar. *Advances in Space Research*, *40*(6), 734–743. https://doi.org/10.1016/j.asr.2007.05.059

Lehmacher, G. A., Scott, T. D., Larsen, M. F., Bilen, S. G., Croskey, C. L., Mitchell, J. D., et al. (2011). The Turbopause experiment: atmospheric stability and turbulent structure spanning the turbopause altitude. *Annales Geophysicae*, *29*, 2327–2339. https://doi.org/10.5194/angeo-29-2327-2011

Liu, A. Z., Roble, R. G., Hecht, J. H., Larsen, M. F., & Gardner, C. S. (2004). Unstable layers in the mesopause region observed with Na lidar during the Turbulent Oxygen Mixing Experiment (TOMEX) campaign. *Journal of Geophysical Research*, *109*, D02S02. https://doi.org/10.1029/2002JD003056

Lombard, P. N., & Riley, J. J. (1996). Instability and breakdown of internal gravity waves. I. Linear stability analysis. *Physics of Fluids*, *8*(12), 3271–3287. https://doi.org/10.1063/1.869117

Lund, T. S., & Fritts, D. C. (2012). Numerical simulation of gravity wavebreaking in the lower thermosphere. *Journal of Geophysical Research*, *117*, D21105. https://doi.org/10.1029/2012JD017536

Lübken, F.-J. (1997). Seasonal variation of turbulent energy dissipation rates at high latitudes as determined by in situ measurements of neutral density fluctuations. *Journal of Geophysical Research*, *102*(D12), 13,441–13,456. https://doi.org/10.1029/97JD00853

Lübken, F.-J., Rapp, M., & Hoffmann, P. (2002). Neutral air turbulence and temperatures in the vicinity of polar mesosphere summer echoes. *Journal of Geophysical Research*, *107*(D15), 4273. https://doi.org/10.1029/2001JD000915

Makhlouf, U. B., Picard, R. H., & Winick, J. R. (1995). Photochemical dynamical modeling of the measured response of airglow togravity waves 1. *Basic model for OH airglow. Journal of Geophysical Research*, *100*, 11,289–11,311.

McComas, C. H., & Bretherton, F. P. (1977). Resonant interaction of oceanic internal waves. *Journal of Geophysical Research*, *82*(9), 1397–1412. https://doi.org/10.1029/JC082i009p01397

Miller, A. D., Fritts, D. C., Chapman, D., Jones, G., Limon, M., Araujo, D., et al. (2015). Stratospheric imaging of polar mesospheric clouds: A new window on small-scale atmospheric dynamics. *Geophysical Research Letters*, *42*, 6058–6065. https://doi.org/10.1002/2015GL064758

Pautet, P.-D., Taylor, M. J., Fritts, D. C., Bossert, K., Williams, B. P., Broutman, D., et al. (2016). Large-amplitude mesospheric response to an orographic wave generated over the Southern Ocean Auckland Islands (50.7°S) during the DEEPWAVE project. *Journal of Geophysical Research: Atmospheres*, *121*, 1431–1441. https://doi.org/10.1002/2015JD024336

Pfrommer, T., Hickson, P., & She, C.-Y. (2009). A large-aperture sodium fluorescence lidar with very high resolution for mesopause dynamics and adaptive optics studies. *Geophysical Research Letters*, *36*, L15831. https://doi.org/10.1029/2009GL038802

Rapp, M., Strelnikov, B., Müllemann, A., Lübken, F.-J., & Fritts, D. C. (2004). Turbulence measurements implications for gravity wave dissipation during the MaCWAVE/MIDAS summer rocket program. *Geophysical Research Letters*, *31*, L24S07. https://doi.org/10.1029/2003GL019325

Satomura, T., & Sato, K. (1999). Secondary generation of gravity waves associated with the breaking of mountainwaves. *Journal of Atmospheric Sciences*, *56*, 3847–3858. https://doi.org/10.1175/1520-0469(1999)056<3847:SGOGWA>2.0.CO;2

Snively, J. B., Pasko, V. P., & Taylor, M. J. (2010). OH and OI airglow layer modulation by ducted short-period gravity waves: Effects of trapping altitude. *Journalof Geophysical Research*, *115*, A11311. https://doi.org/10.1029/2009JA015236

Sonmor, L. J., & Klaassen, G. P. (1997). Toward a unified theory of gravity wave stability. *Journal of the Atmospheric Sciences*, *54*(22), 2655–2680. https://doi.org/10.1175/1520-0469(1997)054<2655:TAUTOG>2.0.CO;2

Staquet, C., & Sommeria, J. (2002). Internal gravity waves: From instability to turbulence. *Annual Review of Fluid Mechanics*, *34*, 559–593.

Strelnikov, B., Rapp, M., Strelnikova, I., Engler, N., & Latteck, R. (2009). Small-scale structures in neutrals and charged aerosol particles as observed during the ECOMA/MASS rocket campaign. *Annales de Geophysique*, *27*, 1449–1456. http://www.ann-geophys.net/27/1449/2009

Sutherland, B. R. (2001). Finite-amplitude internal wavepacket dispersion and breaking. *Journal of Fluid Mechanics*, *429*, 343–380. https://doi.org/10.1017/S0022112000002846

Sutherland, B. R. (2006). Internal wave instability: Wave-wave versus wave-induced mean flow interactions. *Physics of Fluids*, *18*(7), 074107. https://doi.org/10.1063/1.2219102

Swenson, G. R., & Mende, S. B. (1994). OH emissions and gravity waves (including a breaking wave) in all-sky imagery from Bear Lake, Utah. *Geophysical Research Letters*, *21*(20), 2239–2242. https://doi.org/10.1029/94GL02112

Szewczyk, A., Strelnikov, B., Rapp, M., Strelnikova, I., Baumgarten, G., Kaifler, N., et al. (2013). Simultaneous observations of a mesospheric inversion layer and turbulence during the ECOMA-2010 rocket campaign. *Annales Geophysicae*, *31*(5), 775–785. https://doi.org/10.5194/angeo-31-775-2013

Taylor, M. J., Pautet, P.-D., Criddle, N. R., Fritts, D. C., Eckermann, S. D., Smith, S. M., et al. (2019). Large-amplitude mountain waves in the mesosphere observed on 21 June 2014 during DEEPWAVE: 1. Wave amplitudes, scales, momentum fluxes, and environmental sensitivity. *Journal of Geophysical Research: Atmospheres*, *124*. https://doi.org/10.1029/2019JD030932

Theon, J. S., Nordberg, W., Katchen, L. B., & Horvath, J. J. (1967). Some observations on the thermal behaviour of the mesosphere. *Journal of the Atmospheric Sciences*, *24*(4), 428–438. https://doi.org/10.1175/1520-0469(1967)024<0428:SOOTTB>2.0.CO;2

Thorpe, S. A. (1987). Transitional phenomena and the development of turbulence in stratified fluids: A review. *Journal of Geophysical Research*, *92*(C5), 5231–5248. https://doi.org/10.1029/JC092iC05p05231

Thorpe, S. A. (1994). Observations of parametric instability and breaking waves in an oscillating tilted tube. *Journal of Fluid Mechanics*, *261*, 33–45. https://doi.org/10.1017/S0022112094000248

Thorpe, S. A. (2002). The axial coherence of Kelvin-Helmholtz billows. *Quarterly Journal of the Royal Meteorological Society*, *128*(583), 1529–1542. https://doi.org/10.1002/qj.200212858307

Walterscheid, R. L., Gelinas, L. J., Hecht, J. H., & Liu, A. Z. (2013). Instability structures during periods of large Richardson number (Ri > 1/4): Evidence of parametric instability, J. *Journal of Geophysical Research: Atmospheres*, *118*, 6929–6939. https://doi.org/10.1002/jgrd.50514

Williams, B. P., Fritts, D. C., She, C.-Y., & Goldberg, R. A. (2006). Gravity wave propagation through a large semidiurnal tide and instabilities in the mesosphere and lower thermosphere during the winter 2003 MaCWAVE rocket campaign. *Annales de Geophysique*, *24*(4), 1199–1208. www.ann-geophys.net/24/1199/2006/, https://doi.org/10.5194/angeo-24-1199-2006

Witt, G. (1962). Height, structure and displacements of noctilucent clouds. *Tellus*, *14*, 1–18.

Yamada, Y., Fukunishi, H., Nakamura, T., & Tsuda, T. (2001). Breaking of small-scale gravity wave and transition to turbulence observed in OH airglow. *Geophysical Research Letters*, *28*(11), 2153–2156. https://doi.org/10.1029/2000GL011945